“Cocktail”-type catalysis on bimetallic systems for cinnamaldehyde selective hydrogenation: Role of isolated single atoms, nanoparticles and single atom alloys

Jérémy Audevard, Javier Navarro-Ruiz, Vincent Bernardin, Régis Philippe, Anna Corrias, Yann Tison, Alain Favre-Réguillon, Iker Del rosal, I.C. Gerber, P. Serp

"Cocktail"-type catalysis on bimetallic systems for cinnamaldehyde selective hydrogenation: role of isolated single atoms, nanoparticles and single atom alloys

Jérémy Audevard,[a,‡] Javier Navarro-Ruiz,[b,‡] Vincent Bernardin,[c] Régis Philippe,[c] Anna Corrias,[d] Yann Tison,[e] Alain Favre-Réguillon,[c, f] Iker Del Rosal,[b] Iann C. Gerber[b] and Philippe Serp[a,*]

[a] *LCC−CNRS, Université de Toulouse, UPR 8241 CNRS, INPT, Toulouse, France*
[b] *Université de Toulouse, INSA−CNRS−UPS, LPCNO, Toulouse F-31077, France*
[c] *Université Lyon, CP2M, UMR 5128 CNRS - CPE Lyon, 43 boulevard du 11 novembre 1918, F-69100 Villeurbanne, France*
[d] *School of Chemistry and Forensic Science, University of Kent Canterbury, Ingram Building, Room 118, CT2 7NH, UK*
[e] *IPREM CNRS UMR 5254, Université de Pau et des Pays de l'Adour, Pau 64053, France*
[f] *Département Chimie-Vivant-Santé, Conservatoire National des Arts et Métiers, 292 rue Saint Martin, F-75003 Paris, France*

Abstract. Reaching high selectivity at high conversion and high rate in the industrially important selective hydrogenation of α,β-unsaturated aldehydes is a challenging task. Among current approaches reported in the literature, high selectivity towards the unsaturated alcohol or saturated aldehyde is generally achieved at the expense of activity. The use of bimetallic systems can lead either to selectivity or to activity enhancement, but generally not to both. Herein, we show that, for cinnamaldehyde hydrogenation, combining Ni nanoparticles (Ni_{NP}) and Ru single atoms (Ru_{SA}) on CNTs allows improvement of the hydrocinnamaldehyde

selectivity, while obtaining a remarkable activity. The STY of Ru_{SA}-Ni_{NP}/CNT is approximately 60 times higher than that of the Ru_{SA}/CNT and 10 times higher than that of the Ni_{NP}/CNT. Importantly, the resulting catalyst shows 94% selectivity at 99% conversion and a good stability in flow. Insights into the cooperative "cocktail"-type catalysis between Ni_{NP} and Ru_{SA} were revealed from density functional theory calculations.

Keywords: selective hydrogenation, single atoms, ruthenium, palladium, nickel, hydrogen spillover

1. Introduction

Controlling catalyst's selectivity while maintaining its activity is a difficult task, especially in selective hydrogenation reactions of organic substrates. The selective hydrogenation of α,β-unsaturated aldehydes is a representative example that arouses interest both from the academic and industrial sides. First, it can be used to probe geometric, electronic or confinement effects,[1] and second, the corresponding products are widely used in several segments of the chemical industry. Cinnamaldehyde (CAL) is a classical model substrate, and the main hydrogenation products, hydrocinnamaldehyde (HCAL) and cinnamyl alcohol (COL) can be used as pharmaceutical intermediates, chemicals, perfumes or fragrances. The performance of Pd, Ru or Ni supported catalysts have been evaluated for this reaction.[2] Among these metals, Pd is by far the most active, and generally showed high HCAL selectivity (S_{HCAL} > 80%).[3] Ru is less active and is generally preferred to produce COL, although with moderate selectivity.[4] Non-promoted transition metals of the first row such as Ni show low activity and are, as Pd selective, for HCAL production. The selectivity trend

could be correlated with the metal *d*-band width,[5] the larger the *d*-band, the higher the selectivity to the unsaturated alcohol (Ru > Pd ≈ Ni).

An efficient strategy to tune catalytic performance for selective hydrogenation reactions involved the use of bimetallic or dilute alloy catalytic systems.[6, 7] The promotion by addition of a second metal can be explained by: i) geometric/electronic effects; ii) appearance of mixed active sites; and/or iii) a weakening of the M–H bond. Generally, the bimetallic systems combined a metal that can activate H_2 and another one, usually more electropositive, which can improve the catalytic performance. An intimate contact between the two metals is not mandatory as long as hydrogen spillover[8] (diffusion of mobile H species from the metal to the support) can occur, which is the case on reducible oxides,[9, 10] and carbon materials.[11, 12] The exact nature of these H species (atomic $H^{\cdot}$, H^{+}, H^{-}) depends on the nature of the support and is still the subject of studies.[10, 13, 14] The systems involving H-spillover can be classified into four categories (Scheme 1).

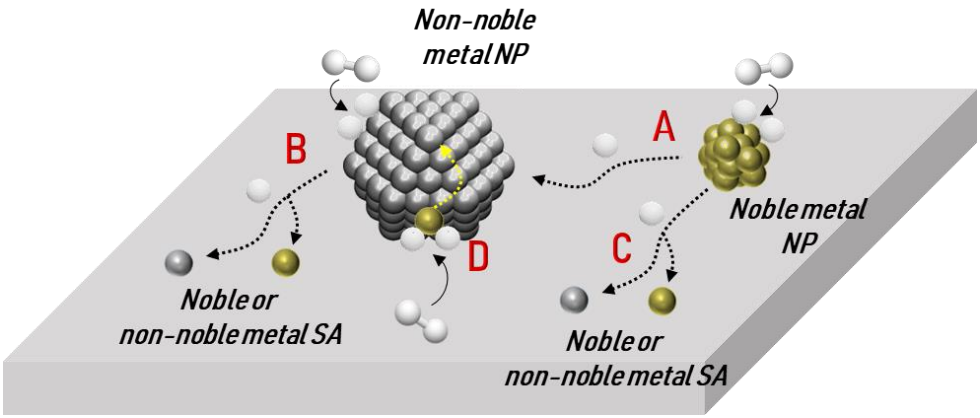

Scheme 1. Different pathways for H-spillover induced cooperative catalysis (see text for description and examples).

The first category follows the *pathway A*. In that case, molecular hydrogen is easily dissociated on a noble metal nanoparticle (NP) and the activated hydrogen reached the

hydrogenating site (a non-noble metal NP) *via* H-spillover. Such mechanism was reported for the selective hydrogenation of CAL to HCAL on Ni-Ir/TiO_2 bimetallic catalysts.[15] Here, the role of Ir_{NP} was to produce activated hydrogen, while CAL hydrogenation occurs on the Ni_{NP}, whose electronic structure is eventually modified upon addition of Ir. This Ni-Ir system was significantly more active than the monometallic ones, but less selective. A similar mechanism was also reported for crotonaldehyde hydrogenation on Pt-Sn bimetallic catalysts, in which Pt_{NP} activated H_2.[16] For the second and third categories (*pathways B* and *C*), metallic NPs are associated to isolated metal single atoms (SAs), resulting in a "cocktail" of catalysts with species of different nuclearity. It is worth mentioning that in that case, the system is not necessarily bimetallic. Although the use of single atom catalysts in (selective) hydrogenation is quite widespread,[17, 18] these catalysts often suffer from difficulties in activating H_2 due to their electrodeficiency resulting from a strong charge transfer with the support. Consequently, specific sites (most of the time a heteroatom such as O[19, 20] or N[21]) should be present at their vicinity on the support for heterolytic H_2 activation to proceed. To overcome this drawback, metal SAs can be associated with metallic NPs that will initiate the H-spillover. *Pathway B* has been proposed for the selective hydrogenation of CAL on Ni/C catalysts, for which Ni_{NP} activated H_2, and H-spillover on the carbon support provided hydride species to Ni_{SA}, on which CAL is selectively hydrogenated into HCAL.[22] *Pathway C* involves the cooperativity between noble metal NPs that activate H_2 and metal SAs that perform the hydrogenation. Although this pathway has not yet been reported for selective hydrogenation reactions, it has already been described on supported Pd catalysts for C=C[23] and C=O[24] bond hydrogenation, as well as for hydrodeoxygenation reactions.[25] In the last category (*pathway D*), the metal SA is directly deposited on a metal NP, resulting in single-atom alloy (SAA) catalyst, for which H-spillover occurs on the surface of the metal NP. This mechanism has been proposed for Pt_{SA}-Cu_{NP} systems that selectively promote the

hydrogenation of C=O bonds in unsaturated aldehydes.[26, 27] For this latter category, the NP can be also a noble metal NP, as for Pt_{SA}-Au_{NP} systems for HCAL production.[28] In these SAA systems, H_2 activation is proposed to occur on Pt_{SA} and hydrogenation on the surface of the NP.

In the continuation of our studies on the cooperative catalysis between metal SAs and NPs[23, 29-32] herein, the catalytic performance of a Ru_{SA}/CNT catalyst (CNT: carbon nanotubes) for CAL hydrogenation in apolar solvent is first evaluated in order to produce HCAL.[4] Then, the catalytic performances of this catalyst were compared compared to the ones of Ru_{SA}-M_{NP}/CNT catalysts (M = Ru, Pd, Ni) that can follow different pathways *(B, C* and/or *D*). The main aim of the present work is to discuss the interaction between the active species as well as the role of the M_{NP} in the Ru_{SA}-M_{NP}/CNT catalysts for selective hydrogenation. Insights into the cooperative catalysis between Ni_{NP} and Ru_{SA} for CAL hydrogenation were revealed from density functional theory calculations.

2. Material and methods

2.1. Carbon nanotube synthesis

The carbon nanotubes were produced by catalytic-CVD in a fluidized bed reactor using ethylene as carbon source. An $AlCoFeO_4$ catalyst was first pre-reduced under hydrogen during 30 min at 650 °C. A typical experiment was carried out with ethylene (600 mL min^{-1}) for 30 min to produce CNTs. The produced CNTs were purified (catalyst dissolution) by an aqueous solution of H_2SO_4 (50 vol%) under reflux for 3 h. Finally, the CNTs were functionalized by a treatment of purified CNTs with HNO_3 under reflux at 140 °C for 3 h. The mixture was then filtered and washed with deionized water until pH ≈ 7. The final product was collected and dried at 120 °C overnight.

2.2. Monometallic catalyst preparation

A dry impregnation method was used to prepare the ruthenium catalyst supported on CNTs (Ru_{SA+NP}/CNT). The desired amount of ruthenium(III) nitrosyl nitrate solution was added to acetone (10 mL) containing 1 g of CNTs to introduce 1.2 % w/w of metal phase. The solution was sonicated at room temperature for 1 h and magnetically stirred overnight. The solution was then filtered and washed with acetone. The resulting solid was dried in an oven at 120 °C overnight. Finally, the 1.2 % Ru_{SA+NP}/CNT catalyst was reduced in a horizontal tube oven under a nitrogen and hydrogen flow (20 vol% H_2) at 300 °C for 2 h (25 °C to 300 °C at 10 °C min^{-1}). The same procedure was followed for the 1.2 % Pd_{NP}/CNT and the 1.2 % Ni_{NP}/CNT catalysts, prepared using palladium(II) nitrate $Pd(NO_3)_2.2H_2O$ and nickel(II) nitrate $Ni(NO_3)_2.6H_2O$, respectively.

For the 1.2 % Ru_{SA}/CNT catalyst synthesis, the process consists in: i) creating carboxylic groups on the CNT support by nitric acid oxidation (step I); ii) decomposing these groups

under an inert atmosphere to produce CO_2, some H_2 and carbon vacancies (step II); and iii) depositing the metal on this defective support (step III).[33] Before the step III, the desired amount of (η^4-1,5-cyclooctadiene)(η^6-1,3,5-cyclooctatriene) ruthenium(0) [Ru(COD)(COT)] was added to 30 mL of purified pentane under an inert atmosphere. Then, the solution was added on the support (step III). The mixture was stirred for 1 h and washed with purified pentane. The solid was dried under vacuum overnight. Finally, the catalyst was treated under a nitrogen and hydrogen flow (20 vol% H_2) at 80 °C for 1 h.

2.3. Bimetallic catalyst preparation

To prepare the bimetallic 2 % $Ru_{SA}Ni_{NP}$/CNT catalyst, the desired amount of nickel(II) nitrate $Ni(NO_3)_2.6H_2O$ was added to an acetone solution (10 mL) containing the Ru_{SA}/CNT catalyst to introduce 1 % w/w of the Ni metallic phase. After sonication (1 h at room temperature) and stirring (overnight at ambient temperature), the sample was filtered, washed with acetone, and dried in an oven at 120 °C. Finally, the 2 % $Ru_{SA}Ni_{NP}$/CNT catalyst was reduced in a horizontal tube oven under a nitrogen and hydrogen flow (20 vol% H_2) at 300 °C for 2 h (25 °C to 300 °C at 10 °C min^{-1}). The same procedure was followed for the 2 % $Ru_{SA}Pd_{NP}$/CNT catalyst using $Pd(NO_3)_2.2H_2O$ as Pd precursor.

2.4. Characterization

The metal content in the catalytic materials was measured by inductively coupled plasma optical emission spectroscopy (ICP-OES) performed on a Thermo Scientific ICAP 6300 instrument.

TEM analyses were performed by using a JEOL JEM 1400 electron microscope operating at 120 kV. The high-resolution analyses were conducted by using a JEOL JEM 2100F microscope equipped with a field emission gun (FEG) operating at 200 kV with a point

resolution of 2.3 Å and a JEOL JEM-ARM200F Cold FEG operating at 200 kV with a point resolution of > 1.9 Å. The particle size distribution was determined through a manual measurement of enlarged micrographs from different areas of the TEM grid (at least 300 particles). The SA/NP ratio (a number ratio) was measured from the STEM–HAADF analyses (around 30 STEM micrographs) of 5000-10000 elements, according to the sample.

The X-ray absorption spectra were recorded on the B18 beam line at the DIAMOND synchrotron (Oxfordshire, UK). The samples, in the form of powder, were diluted with polyvinylpyrrolidone (PVP) in an appropriate concentration inside a glove box and pressed to form a pellet, which was then sealed in an aluminum pouch to avoid any oxidation. Spectra at the Ru K-edge were collected at room temperature in fluorescence mode using a Si(311) monochromator. The monochromator energy scale was calibrated via a third ion chamber with a reference foil. The data analysis was performed using the ATHENA and ARTEMIS software.[34] With ATHENA, the absorption edge, E_0, is determined, and the absorption due to the isolated atom is subtracted, by fitting the pre-edge and post-edge regions to obtain $\chi(k)$. The software ARTEMIS is used to perform the fit of the EXAFS region to scattering models in R-space obtained by FEFF, validated on standard compounds; the amplitude reduction factor S_0^2 was fixed to 0.9 during fitting. The number of fitted parameters was always lower than the number of independent points. The samples were also analyzed by X-ray photoelectron spectroscopy using a VG Escalab MKII spectrophotometer, which operated with a non-monochromatized Mg K_α source (1253.6 eV).

2.5. Cinnamaldehyde hydrogenation in stirred tank batch reactor

Hydrogenation reactions were performed in a Top Industrie high pressure and temperature stainless steel autoclave with a temperature/stirring/pressure controlling system. In a typical experiment, a mixture of catalyst (0.004 mmol), nonane (1.5 mmol, 200 mg, as internal

standard), trans-cinnamaldehyde (4.0 mmol, 528 mg), and 30 mL of dioxane as a solvent was ultrasonicated for 5 min, and then transferred into the high-pressure autoclave. The autoclave was purged 3 times with N_2. Then, the autoclave was heated to 100 °C and pressurized with 20 bar of H_2, setting the stirring rate at 1000 rpm. The reaction test duration was 6 hours. Samples of the reaction mixture were taken periodically. The products were analyzed on a PerkinElmer gas chromatograph equipped with Elite–5MS capillary column (30 m x 0.32 mm x 0.25 mm) with a flame ionization detector. For recycling experiments, the same procedure was followed. Between each cycle, the catalyst was separated by filtration and washed three times with dioxane before being reused. TOF were calculated based on total surface metal considering the presence of metal single atoms and when relevant metallic NPs. The metallic dispersion for NPs was calculated from a universal mathematical relationship between the average relative size of metallic crystallites and their dispersion.[35]

2.6. Coating of open-cell solid foam substrates with RuNi/CNT catalyst

Metallic open cell solid foams (OCSF) NiCr 2733 from RECEMAT (3010 m^2 m^{-3} geometrical specific surface and 92 % porosity determined thanks to X-ray tomography) were precisely cut into cylinders (diameter: 4.3 mm and length: 25.0 mm) through electric arc discharge machining. These objects were washed in acetone under sonication for 15 min at room temperature and dried overnight. Then, the cleaned OCSF substrates were heated (5 °C min^{-1}) up to 600 °C under air atmosphere, followed by a 4 h plateau at this temperature. Natural cooling down to room temperature completed the activation of the objects. A pre-reduced 2 wt.% $Ru_{SA}Ni_{NP}$/CNT catalyst (300 °C, H_2 atmosphere, 2h) was used to prepare a 60 g L^{-1} suspension in water accordingly to the following procedure adapted from previous works[36]: in a planetary ball mill (Retsch PM100), 20 mL of deionised water are mixed with 0.4 g of dextrin (Sigma-Aldrich) for 5 min at 300 rpm. Then, 0.4 g of triton X (Sigma-Aldrich) are added and mixed again for 5 min at 300 rpm. Finally, 1.2 g of the RuNi/CNT

catalyst are put in the mill and the mixture was ball-milled for 45 min at 500 rpm (3x15 min with change in rotational direction). This suspension was used to dip coat a series of activated foam cylinders. Excess suspension was removed by a careful air flow through the coated structures. The samples were then dried overnight at 80 °C and weighed. A similar catalyst content of 29.0 ± 3.0 $g_{RuNi/CNT}$ L_{foam}^{-1} was obtained for the different foam pieces, corresponding to an estimated mean layer thickness of 15 µm (assuming a homogeneous coverage). Coating homogeneity was characterized through optical microscopy (Keyence VHX-6000) and SEM-EDX measurements help to confirm the mean thickness of the coatings. Additional characterizations of the fresh coated catalysts were performed using HAADF-STEM to check the impact of coating procedure on Ru-Ni active particles (size and spatial distribution).

2.7. Cinnamaldehyde hydrogenation in continuous flow reactor

4 coated foam objects were inserted in a home-made stainless steel milli-reactor (4.4 mm internal diameter, length of active zone of 100 mm) corresponding to an involved mass of 42 mg of RuNi/CNT catalyst. The reactor was operated in co-current up-flow of gas and liquid. The liquid solution is precisely fed thanks to a HPLC pump (Shimadzu, LC2 0 AD) and the H_2 gas flow is controlled thanks to a mass-flow controller (Bronkhorst Elflow Prestige). Gas and liquid feeding lines met at a simple T-junction upstream of the reactor. The liquid is preheated in a stainless-steel loop with a thermoregulated oil bath to the desired temperature before entering the reactive zone. Temperature and pressure were controlled and monitored (Labview) through a regulated electrical oven and an equilibar back pressure regulator, respectively. Downstream, gas-liquid separation and liquid collection and sampling were made through a simple gravity driven separator. Liquid phase analysis was made offline periodically thanks to a GC-FID equipment (Shimadzu Nexis GC2030).

In the continuous experiments, the catalytic foam objects were conditioned *in situ* under H_2 flow (100 N mL min^{-1}) at the reactor temperature and pressure (160 °C and 20 bar) for 15 min. Then, the H_2 gas flow rate was set to 20 N mL min^{-1} and the liquid was set to the desired flow rate. The liquid mixture consists of a solution of 0.133 M of CAL (Sigma Aldrich, 99%) and 0.032 M of tetradecane (Sigma Aldrich, 99%), used as internal standard, was prepared in absolute ethanol (Sigma Aldrich) as solvent. Liquid flow rates varying between 0.2 and 1.0 mL min^{-1} have been experienced, corresponding to contact times between 5.1 and 25.5 h mol_{CAL}^{-1} mol_{Ni+Ru}^{-1}.

2.8. Test to assess hydrogen spillover

To check for the H-spillover, WO_3 is used to diagnose the activation of H_2 in the various catalysts, because the spilled-over hydrogen migrates and readily reacts with the yellow WO_3 to form dark blue H_xWO_3.[37] Samples made with 1 g of WO_3 were mixed (or not) with 5 mg of catalyst and treated with H_2 (100 mL min^{-1}) at 100 °C for 2 min.

2.9. Computational details

Periodic Density Functional Theory (DFT) calculations were performed using the *ab initio* plane-wave pseudopotential approach, as implemented in the Vienna Ab initio Simulation Package (VASP; version 5.4).[38, 39] The exchange−correlation potential was approximated with the generalized gradient approximation to the Perdew-Burke-Ernzerhof functional[40] and van der Waals interactions were taken into account through the D3 correction method of Grimme *et al*.[41] The core electrons were modeled using the Projector Augmented Wave (PAW) approach,[42, 43] and the valence monoelectronic states were expanded using a plane wave basis set with a cutoff energy of 450 eV. Partial occupancies were estimated with a Gaussian smearing (σ) of 0.05 eV during all relaxations and extrapolating the energies to σ = 0.00 eV. As recently computationally modeled and described in our group,[44] the supported

metal catalyst consists of an O-functionalized graphene (including experimentally probed abundant oxygen functional groups and point defects) as carbon support, together with a single Ru atom in a single vacancy and a small M_{13} nanoparticle (M = Ru, Pd, Ni) as supported metal catalysts, the latter being hydrogenated with a ratio between adsorbed hydrides and surface metal atoms above unity. Γ-Centered (3×3×1) *k*-point mesh generated using the Monkhorst–Pack method was employed,[45] with spin polarization on the nickel-containing systems. A vacuum region by at least 10 Å between the periodically repeated slabs was added to eliminate spurious interactions, and a dipole correction along the *z*-direction has been considered.[46] All structures were optimized until forces were less than 0.015 eV $Å^{-1}$. Transition states were first located using the Climbing Image version of the Nudged Elastic Band, CI-NEB, method,[47, 48] and then properly optimized using the Quasi-Newton algorithm. Finally, they were proven to show a single imaginary frequency by the diagonalization of the numerical Hessian matrix with a step of 0.015 Å in both positive and negative directions of each coordinate.

3. Results and discussion

This study involves the preparation of catalysts based on isolated SAs, metallic NPs or mixtures of SAs and NPs with metal loading conventionally used for the CAL hydrogenation reaction (1-2% w/w). The preparation and characterization of this type of catalysts on carbon supports is not trivial. First, most carbon supports present in variable quantities sites capable of stabilizing SAs.[49] Consequently, most carbon-supported NP-based catalysts (including commercial ones) contain SAs, which can be easily visualized by aberration-corrected scanning transmission electron microscopy (AC-STEM).[50] On the other hand, the preparation and characterization of catalysts containing exclusively SAs with significant metal loading (≥ 1 % w/w) is difficult.[51] In particular, the presence of clusters in such catalysts is not always easy to demonstrate, even by combining several techniques, such as high-angle annular dark-field STEM imaging (HAADF-STEM), EXAFS, and XPS (DRIFTS analysis of carbon surfaces coupled to a probe molecule proves to be very challenging).[52]

3.1. Monometallic Ru_{SA}/CNT and Ru_{SA+NP}/CNT systems

A 1.2 % Ru_{SA}/CNT catalyst is prepared by a reported method that involves creating carbon vacancies on the CNT support to stabilize the Ru_{SA}.[33] For this catalyst, the (η^4-1,5-cyclooctadiene)(η^6-1,3,5-cyclooctatriene) ruthenium(0) [Ru(COD)(COT)] precursor is used to deposit ruthenium. ICP-OES analysis showed a metal content of 0.94 % w/w. The sample is characterized by HAADF-STEM, XPS, and EXAFS. Fig. 1a shows a representative HAADF-STEM image of the catalyst (lower resolution images are shown in Fig. S1(a-b)). This catalyst contains almost exclusively Ru_{SA} (92 at%, see Fig. S1(c-d) for NP size distributions based on total number of NPs and total number atoms[53]). In addition to Ru_{SA}, very few clusters presenting a mean size of 0.8 nm are detected (number ratio Ru_{SA}/Ru_{NP} = 201). EDX analysis

demonstrates that the Ru species are homogeneously distributed on the CNT support (Fig. S2).

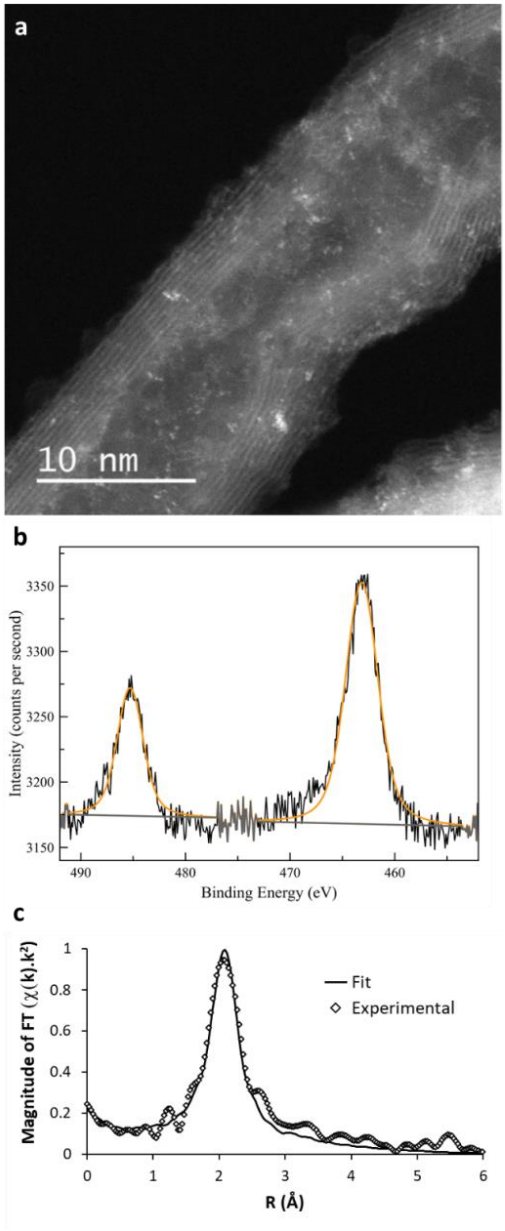

Figure 1. Characterizations of the Ru_{SA}/CNT catalyst (**a**) HAADF-STEM image (scale bar = 10 nm). (**b**) High-resolution Ru 3*p* XPS spectrum. (**c**) Fourier transform magnitude of the experimental Ru K-edge EXAFS $k^2\chi(k)$ and fit results (phase-shift corrected).

XPS analysis is performed with introduction of the Ru_{SA}/CNT sample by a vacuum transfer cell from a glove box under a controlled argon atmosphere, whereby any oxidation of the

sample by air can be excluded. The Ru 3*p* binding energies at 463.2 and 485.3 eV (Fig. 1b) are exceedingly high to correspond to Ru^0 on the carbon support (Ru $3p_{3/2}$ = 461-462 eV[54, 55]), and should be associated to a significant charge transfer from Ru to each of the neighboring C atoms of the support. First-principles studies are carried out to model and describe the geometric and electronic properties of O-functionalized graphene (as model support) decorated with metal NPs and/or metal SAs.[44] In this case, the Ru-supported catalyst model (Fig. 2) is used to interpret the XPS results obtained with the Ru_{SA}/CNT sample.

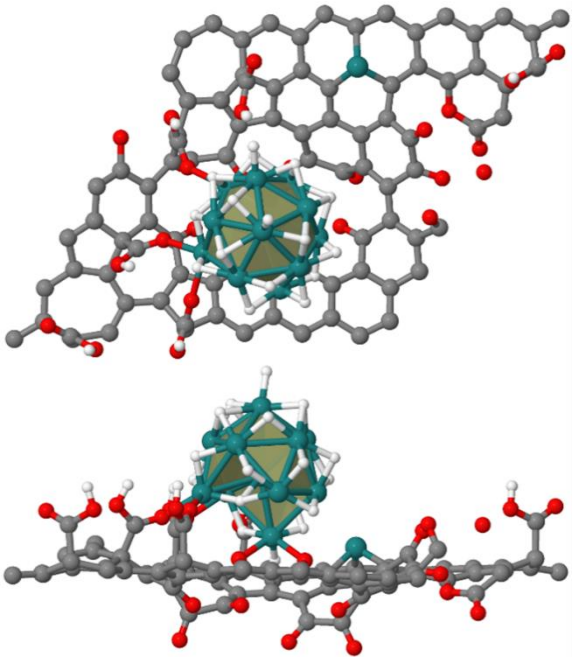

Figure 2. Top and side views of atomistic structure of the Ru_{SA+NP} catalyst model. Atomic Color Scheme: Ru (Celadon Green); O (Candy Apple Red); C (Philippine Gray); H (White).

Analyzing the electronic distribution, a partial atomic charge around +0.9|*e*| is observed for a Ru_{SA} anchored to a single vacancy; highlighting the Ru-to-C charge transfer (see Fig. S3 for the detailed characterization of the Ru_{SA+NP} system).

To gain insight into the dispersion of the Ru species on the Ru_{SA}/CNT catalyst, the coordination environment of Ru is investigated using EXAFS (Fig. 1c). The sample shows only one shell centered around 2.1 Å and no detectable peak due to Ru-Ru interactions which would appear at 2.6-2.7 Å, where only termination ripples can be observed. These results are indicative of Ru_{SA} or very small clusters. The EXAFS data were fitted with a single coordination sphere of C atoms to keep the number of fit parameters to a minimum. The Ru–C bond coordination numbers in this coordination sphere are estimated to be 7.0 at a distance of 2.12 Å, suggesting that the Ru_{SA} lies on a Stone-Wales defect (5775 pair).[56] However, a simplified atomistic model (Model-I, see Fig. S4a) shows that Ru_{SA} initially in the 7-membered ring converges towards a CN = 5 at a distance of 2.16 Å, as well as being thermodynamically infeasible (binding energy of +50.2 kcal·mol^{-1}). Therefore, other more stable models with CN as close to 7 as possible are explored, with Ru_{SA} in a multiple vacancy of the O-functionalized carbon support (Model-II to -IV, see Fig. S4(b-d)). The thermodynamically more stable model, with Ru_{SA} in a single vacancy of the same carbon support, is also studied (Model-V, see Fig. S4e). The DFT models have been used in ARTEMIS[32] to generate FEFF paths to be compared with the experimental EXAFS data as shown in Fig. S5. The Ru–O/Ru–C distances in the Model-I and Model-IV are the ones that give the best agreement with the experiment. The distances in Model-V do not seem enough compatible with the experimental EXAFS data, since there is a large discrepancy between the oscillations produced by the model with those of the experiment, which are in phase opposition. Thus, due to the average information provided by the EXAFS technique, the coexistence of Model-I, Model-IV, and Model-V is feasible, the latter being the minority species compared to the first two. Because of the steric hindrance observed around the metal center in Model-I and Model-IV, Model-V is the most suitable model to carry out the

selective hydrogenation of CAL (further details about this choice will be provided at the end of this section).

The selective hydrogenation of CAL is performed on the 0.94 % Ru_{SA}/CNT catalyst at 100 °C under 20 bar of H_2 in dioxane. Besides the main products COL and HCAL, further hydrogenation leads to the formation of hydrocinnamyl alcohol (HCOL). Diacetal formation is not observed, since it requires the use of alcoholic solvents.[57] The catalytic performances are presented in Table 1. This catalyst shows very low activity for CAL hydrogenation at 100 °C, with a TOF_{1h} of 8 h^{-1} and a S_{HCAL} of 73% at 5% conversion. The lack of reactivity of the Ru_{SA}/CNT catalyst can be explained by the fact that electron-deficient Ru_{SA} are not able to dissociatively chemisorb H_2. In fact, the coordination of H_2 is feasible with an adsorption energy of up to -12 kcal·mol^{-1}, but neither the homolytic dissociation of H_2 on the Ru atom alone (H–Ru–H) nor the heterolytic one by Ru_{SA} and adjacent C atoms (RuH+CH) are achieved. While the former gives H_2 recombination, the latter is not favorable from thermodynamics, with reaction energies in the range of 4-28 kcal·mol^{-1} (see Fig. S6a). Therefore, to improve the reactivity of Ru_{SA} *via* H-spillover, the reactivity of Ru_{SA} combined with Ru_{NP} deposited on the same support is first examined. A catalyst containing a mixture of Ru_{SA} and Ru_{NP} is prepared from a solution of ruthenium(III) nitrosyl nitrate. HAADF-STEM analysis of this 1.21 % Ru_{SA+NP}/CNT catalyst shows: 8 at% Ru_{SA}, a ratio Ru_{SA}/Ru_{NP} = 5, and a Ru_{NP} size = 1.1 nm (Fig. S7). The use of this catalyst allows an improvement of activity (TOF_{1h} = 181 h^{-1}) but not of selectivity (S_{HCAL} = 72%).

Table 1. Catalyst performance for cinnamaldehyde hydrogenation.

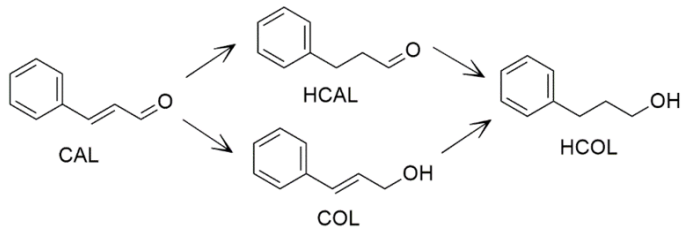

Catalyst	NP size (nm)	Ratio SA/NP	CAL conversion at 1 h (%)	STY (h^{-1})[a]	TOF (h^{-1})[b]	S_{20} (%)[c]		
						HCAL	HCOL	COL
0.94 % Ru_{SA}/CNT	0.72 ± 0.05	201	0.6	8	8	73[c]	13[c]	14[d]
1.21 % Ru_{SA+NP}/CNT	1.15 ± 0.46	5	15.2	154	181	72	6	22
0.99 % Pd_{NP}/CNT	1.54 ± 0.47	3	97.8[d]	4800[e]	7130[e]	84.3	12.3	3.4
2 % $Ru_{SA}Pd_{NP}$/CNT	1.87 ± 1.22	8	74.1[d]	3085[e]	5406[e]	90.4	8	1.6
1.2 % Ni_{NP}/CNT	9.56 ± 2.87	12	4.7	46	307	91.8	8.2	0
2 % $Ru_{SA}Ni_{NP}$/CNT	1.29 ± 0.49	17	53.8	487	637	94.8	5.2	0

[a] STY (mol_{CAL} mol_{metal}^{-1} h^{-1}) at 1 h reaction. [b] TOF (mol_{CAL} $mol_{surf.metal}^{-1}$ h^{-1}) at 1 h reaction. [c] Selectivity at 20% conversion. [d] At 5% conversion. [e] At 15 min reaction time.

For H-spillover-induced cooperative catalysis to operate, H-spillover from Ru_{NP} to Ru_{SA} should be feasible. However, the H-spillover on the Ru_{SA+NP} system is unfavorable from a thermodynamic point of view. All H atoms from Ru_{NP} susceptible of experiencing spillover (*i.e.*, located close to an oxygenated functional group) were tested, the reaction energies obtained being positives and ranged from 3 to 12 kcal·mol^{-1} (see Fig. S6b for a detailed description). Since it is not possible to activate H_2 on Ru_{SA} and H-spillover from Ru_{NP} to Ru_{SA} is hampered, Ru_{SA} in the Ru_{SA+NP}/CNT catalyst should be poorly active for hydrogenation due to the lack of Ru_{SA}-H species. For this reason, the hydrogenation of CAL on Ru_{SA} is not computationally studied. The absence of H-spillover on this catalyst was also experimentally evidenced. Spilled over H species readily reacts under mild conditions with WO_3 (yellow powder) to form dark blue H_xWO_3.[58] As shown in the photographs of Fig. S8a, the WO_3 alone exhibited an unchanged color after H_2 treatment for 10 min. at 100 °C. When mixed with the Ru_{SA+NP}/CNT catalyst, no change of color is noticed (Fig. S8b). As the H-spillover cannot operate between Ru_{NP} and Ru_{SA} on the CNT support, the performance of the 1.21 % Ru_{SA+NP}/CNT catalyst should be attributed mainly to Ru_{NP}. The reaction mechanism for the semi-hydrogenation of CAL to HCAL and COL on Ru_{NP} is studied by DFT (the energy profile is summarized in Fig. S9, and Fig. S10 shows the structures corresponding to the reaction profile). The CAL adsorption can occur through the C=C or the C=O double bond, the first mode being especially favorable (-57 and -45 kcal·mol^{-1}, respectively). The hydrogenation process is thermodynamically favorable for the two possible products, with reaction energies ranging from -19 for COL to -28 kcal·mol^{-1} for HCAL. The kinetically most energy-demanding step according to the two preferred mechanisms is always the first H insertion, with average energy barriers around 25 kcal·mol^{-1}. This could explain the small increase in activity (at 100 °C the reaction can occur) as well as the still not too high selectivity

(Ru_{NP} could give both products because both are energetically similar). Even so, it seems that Ru_{NP} gives HCAL as the main hydrogenation product, since the species are more strongly adsorbed, making the H-insertions surmountable. The TOF obtained with this catalyst (TOF_{1h} = 181 h^{-1}) is in the same range as those obtained with Ru/C catalysts containing Ru_{NP} for CAL hydrogenation (15-450 h^{-1}).[4] Consequently, *pathway C* (Scheme 1) cannot operate between Ru_{NP} and Ru_{SA} on carbon support. Finally, the H-spillover operability was also verified for the different models of Ru_{SA} anchored in an MV proposed previously (Fig. S4). On the one hand, through an energy decomposition analysis for Ru_{SA} in a SV (*Model-V* and Ru_{SA+NP} system, see Fig. S11), it is found that the only model capable of experiencing H-spillover from thermodynamics is *Model-II*. However, neither of the two coordination modes for CAL (C=C or C=O) is favorable on the Ru_{SA}–H species of this model. On the other hand, the *Model-IV* does allow the adsorption of CAL (only through the aldehyde function) but the H-spillover is not favorable on this model (around 13 kcal·mol^{-1}). Therefore, the most thermodynamically stable model with Ru_{SA} located in a SV (*Model-V*) is the only model that leads to the formation of the Ru_{SA}–H species and to the coordination of CAL. This model therefore seems the most relevant to explore the reactivity of the system.

As *pathway C* cannot operate between Ru_{NP} and Ru_{SA}, cooperative catalysis with two other metals associated in the form of NPs to Ru_{SA}, palladium and nickel, is therefore addressed in the following.

3.2. Heterobimetallic $Ru_{SA}Pd_{NP}$/CNT and $Ru_{SA}Ni_{NP}$/CNT systems

Palladium is much more active than ruthenium for this reaction and usually produces HCAL with good selectivity. Supported Pd catalysts are also known to promote H-spillover,[59] and

since this phenomenon has been reported for a Pd-Ru/C catalyst,[60] a cooperativity between Pd_{NP} and Ru_{SA} could be expected. It is verified by DFT that, in the case of the $Ru_{SA}Pd_{NP}$ system, the H-spillover process can occur due to the slightly favorable thermodynamics, between -4 and -9 kcal·mol^{-1} depending on the H atom (see Fig. S12 for the characterization of $Ru_{SA}Pd_{NP}$ catalyst model, and Fig. S13 for a detailed description on the computed values). A 1.2 % Pd/CNT catalyst is first prepared from palladium nitrate (4 at% Pd_{SA}, ratio Pd_{SA}/Pd_{NP} = 3, Pd_{NP} size = 1.5 nm, Fig. S14) to assess the reactivity of Pd_{NP}. Considering the very low concentration of Pd_{SA} in this sample, it is named 1.2 % Pd_{NP}/CNT. This catalyst is very active for CAL hydrogenation (TOF_{15min} = 7130 h^{-1}), and as expected it presented a high S_{HCAL} of 84.3 %. Hydrogenation of CAL at 150 °C and 50 bar on 5%Pd-1% Ru/CNT catalysts containing metallic NPs has already been reported in the literature.[61] On this bimetallic catalyst, the conversion of CAL and the S_{COL} were better than on the monometallic counterparts. To probe for possible cooperativity between Pd_{NP} and Ru_{SA}, 1 % Pd w/w palladium is deposited from Pd nitrate on the 0.94 % Ru_{SA}/CNT catalyst to produce 2 % $Ru_{SA}Pd_{NP}$/CNT (0.82% Ru + 1.03% Pd from ICP). This catalyst shows 1.7 at% Ru_{SA}, a ratio SA/NP ratio of 8, and a Pd_{NP} size of 1.9 nm (Fig. S15). In such a heterobimetallic catalyst, Ru_{SA} should act as reactive nucleation centers for Pd deposition. Thus, in addition to predeposited Ru_{SA}, many Pd_{NP} are found to be associated to Ru_{SA} (Fig. S16 for EDX analysis). Consequently, both *pathways C* (Pd_{NP}+Ru_{SA}) and *D* (Ru_{SA}@Pd_{NP} SAA catalyst) could coexist in this system. XPS analysis performed on this sample did not allow distinguishing isolated Ru_{SA} from Pd_{NP}@Ru_{SA} SAA. Indeed, the Ru 3*p* spectrum of this sample (Fig. 3, blue line) is similar to that of the Ru_{SA}/CNT catalyst (Fig. 3, black line), pointing either to the absence of a significant charge transfer in the SAA or to a high proportion of isolated Ru_{SA} in the sample It was experimentally verified that H-spillover is operative on this catalyst (Fig.

S8c). The combination of Ru_{SA} and Pd_{NP} allows S_{HCAL} to be increased, reaching 90.4 %. The TOF decreased (TOF_{15min} = 5406 h^{-1}) compared to the 1.2 % Pd_{NP}/CNT catalyst (TOF_{15min} = 7130 h^{-1}), suggesting lower activity for Ru_{SA} compared to Pd_{NP} or activated Pd_{SA} (that is, Pd_{SA}–H species after an H-spillover mechanism from Pd_{NP}). If it appears that cooperative catalysis induces a better selectivity for HCAL thanks to Ru_{SA} (present on the support or on the Pd_{NP}), the very high activity of Pd_{NP} makes it difficult to decide on the activity of the Ru_{SA}-H species. For this, a metal with an activity significantly lower than Pd is used for the hydrogenation of CAL: nickel. Although less efficient than Pd because of a stronger M-H bond,[62] carbon-supported Ni catalysts are also active for H-spillover.[63-66]

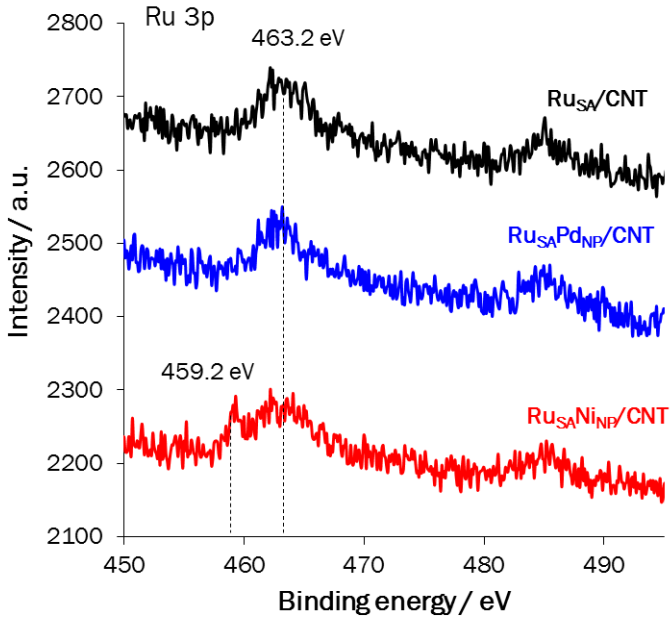

Figure 3. Comparison of the Ru 3*p* XPS spectra of the Ru_{SA}/CNT, $Ru_{SA}Pd_{NP}$/CNT, and $Ru_{SA}Ni_{NP}$/CNT catalysts.

It was independently verified by DFT that H-spillover can operate in the $Ru_{SA}Ni_{NP}$ system, resulting in a thermodynamically favorable process with reaction energies between -4 and -7 kcal·mol^{-1}, very similar to the values obtained for the $Ru_{SA}Pd_{NP}$ system (see Fig. S17 for the characterization of $Ru_{SA}Ni_{NP}$ catalyst model, and Fig. S18 for a detailed description on the computed values). It is worth noting that in systems where Ru and Ni are directly associated, it has been reported that it is Ru that activates H_2 to provide H species to Ni, which contributes to higher catalytic performance.[67-70] For CAL hydrogenation on Ni-Ru systems, contrasting results were reported. 99% Ni-1% Ru bimetallic NPs, in which small amounts of Ru were deposited by galvanic displacement on the Ni_{NP} surface, were investigated by Zhang *et al*.[71] This catalyst, which could contain Ru_{SA} on Ni_{NP} (SAA type) shows, at 100 °C and 15 bar, a conversion similar to that obtained with Ni_{NP}, but is more selective towards HCAL (S_{HCAL} = 79.1 % for the Ni-Ru system and 54.1 % for Ni_{NP}). Surprisingly, at 150 °C and 10 bar, a selectivity of 97.5 % to HCOL was reported for a Ni-Ru catalyst containing magnesium/aluminum hydrotalcite.[72]

A 1 % Ni/CNT catalyst (1.02 % Ni from ICP) is prepared from nickel nitrate (≈ 0 at% Ni_{SA}, ratio Ni_{SA}/Ni_{NP} = 12, Ni_{NP} size = 9.5 nm, Fig. S19). The low Ni dispersion on this catalyst is in accordance with mean Ni_{NP} size reported in the literature for Ni/CNT catalysts.[73-75] This catalyst shows low activity (TOF_{1h} = 306 h^{-1}), and presented a high S_{HCAL} of 91.8%, in accordance with the reactivity of Ni/C catalysts for CAL hydrogenation.[76-78] To probe cooperativity between Ni_{NP} and Ru_{SA}, 1 % Ni w/w nickel nitrate is deposited on the 0.94 % Ru_{SA}/CNT catalyst to yield 2 % $Ru_{SA}Ni_{NP}$/CNT (0.72% Ru + 1.07% Ni from ICP). A loss of Ru occurs during catalyst preparation. Ruthenium leaching could be due to dissolution with nitrate salts of Ru clusters presenting Ru atoms of high surface energy during the impregnation

procedure. This catalyst shows 3 at% Ru_{SA}, a ratio SA/NP = 17, and a Ni_{NP} size = 1.3 nm (Fig. S20). We do not believe that Ni_{SA} could be easily formed during the preparation of this bimetallic catalyst since the stabilizing sites for SAs (the carbon vacancies) are already occupied by the Ru_{SA}, or have been passivated during the reduction of the Ru_{SA}/CNT catalyst. In addition, galvanic replacement is unlikely as the Ru_{SA} are already oxidized, and for Ni it will be favored in the opposite configuration.

The occurrence of H-spillover on this catalyst was experimentally evidenced at 100 °C. As shown in the photographs of Fig. S8d, when mixed with the $Ru_{SA}Ni_{NP}$/CNT catalyst, the WO_3 changed of color upon H_2 treatment, pointing to its reduction to H_xWO_3 by H spillover species. The color change is however much less marked than in the case of the $Ru_{SA}Pd_{NP}$/CNT sample (Fig. S8c). In this heterobimetallic system, the Ru_{SA} act as nucleation centers for Ni deposition. The first consequence of a high nucleation rate is that Ni_{NP} are significantly smaller in $Ru_{SA}Ni_{NP}$/CNT catalyst (1.3 nm) than in the Ni_{NP}/CNT one (9.5 nm). The EDS elemental mappings of the $Ru_{SA}Ni_{NP}$/CNT catalyst present on Figure 4a and Figure S21 illustrate a highly dilute Ru phase on Ni_{NP}, suggesting the presence of Ru-Ni SAA ($Ru_{SA}@Ni_{NP}$). The EDS elemental mapping of quasi SAA involving Pd on Ni_{NP} shows a much higher contribution of Pd,[79] compared to the Ru contribution we have measured. In addition, a number of atom-sized bright spots (highlighted by the yellow circles on Figure 4a,b) have been attributed to individual Ru atoms distributed on the surface of Ni_{NP}.[80] Although we cannot ruled out the presence of low nuclearity Ru clusters/patches on Ni nanoparticles, the STEM-HAADF micrographs clearly indicate the presence of Ru_{SA} on Ni_{NP}. Thus, the 2 % $Ru_{SA}Ni_{NP}$/CNT catalyst contains a cocktail of isolated Ru_{SA} and Ru-decorated Ni_{NP}, $Ru_{SA}@Ni_{NP}$ (see Fig. S22 for representative HAADF-STEM images).

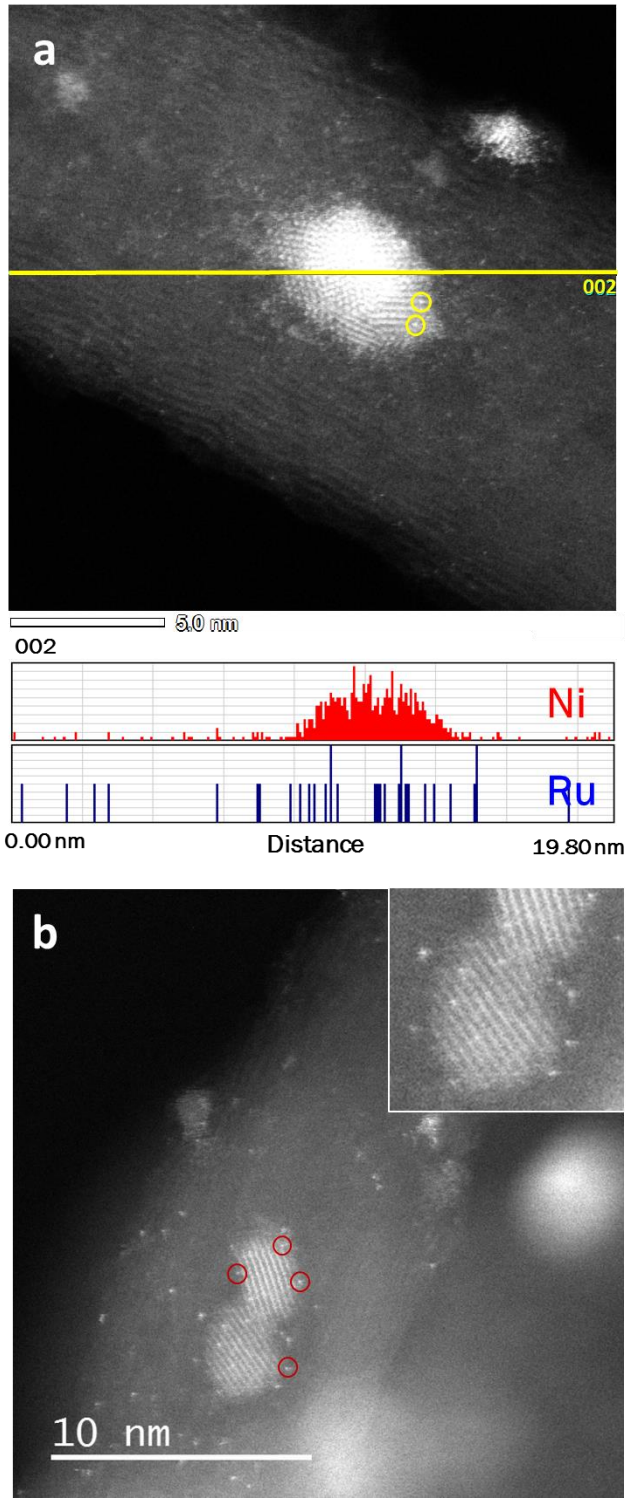

Figure 4. (**a**) STEM-EDX analysis of the $Ru_{SA}Ni_{NP}$/CNT catalyst. (**b**) STEM-HAADF micrograph of the $Ru_{SA}Ni_{NP}$/CNT catalyst.

Consequently, both *pathways B* (Ni_{NP}+Ru_{SA}) and *D* (Ru_{SA}@Ni_{NP}, SAA catalyst) could proceed in this system. XPS analysis performed on this sample allows distinguishing isolated Ru_{SA} from Ru_{SA}@Ni_{NP} SAA. In fact, the Ru 3*p* spectrum of this sample (Fig. 3, red line) is different to that of the Ru_{SA}/CNT catalyst (Fig. 3, black line). For the $Ru_{SA}Ni_{NP}$/CNT catalyst, two species are present, the isolated Ru_{SA} showing a Ru $3p_{3/2}$ binding energy at 463.2 eV as in the Ru_{SA}/CNT catalyst, and a new species at 459.2 eV. This new peak can be attributed to Ni_{NP}-interacting Ru species in SAA. It is worth noting that the significant binding energy shift compared to what is expected for the Ru^0 species on carbon (Ru $3p_{3/2}$ = 461-462 eV[54, 55]) points to a significant charge transfer from Ni_{NP} to the Ru atoms ($Ru^{\delta-}$ species). The presence of electron-rich Ru species has already been reported in the case of the Ni-Ru[81, 82] and Co-Ru[83] bimetallic systems, as well as in the case of Ru-Ni SAA catalysts.[80] Thus, in a 0.5 %Ru-5 %Ni/MMT catalyst (particle size in the range of 1.5-4.5 nm) in which each Ru_{SA} was surrounded by three or four Ni atoms, the Ru $3p_{3/2}$ binding energy was measured at 458.8 eV.[81] The Ni 2p high-resolution XPS spectrum (Fig. S23) shows mainly the presence of nickel oxide (NiO and/or Ni_2O_3),[84, 85] with a binding energy at 855.6 eV. This high binding energy can be explained by the high sensitivity towards oxidation of small Ni particles due to the most reactive low-coordinated metallic Ni sites,[86] and/or by the charge transfer from Ni to Ru and/or from Ni to carbon.[87] The single-atom alloy catalyst model is based on the previous $Ru_{SA}Ni_{NP}$ system by replacing one Ni atom of the Ni_{NP} with one of ruthenium, resulting in a Ni_{NP}-coated surface Ru (the formation energy, E_{form}, of each possible Ni–Ru exchange is presented in Fig. S24). The thermodynamics of all these substitutions is favorable, so the formation of this type of SAA model can take place. According to the calculations, it is determined that the most stable configuration occurs with the Ru atom located in the upper-middle part of the Ni_{NP} (*Ni146*

configuration). Analyzing the electronics of this $Ru_{SA}Ni_{NP}$ SAA system (see Fig. S25 for atomistic structure and charge distribution), a partial atomic charge around +0.8 and +1.5|*e*| is observed for Ru_{SA} and the $Ru_{SA}@Ni_{NP}$ species in SAA, respectively. The difference comes mainly from a charge transfer by the surrounding Ni atoms, in addition to the presence of hydrides species on the nanoparticle surface.

The 2 % $Ru_{SA}Ni_{NP}$/CNT catalyst shows an activity (TOF_{1h} = 637 h^{-1}) much higher than that of 0.94 % Ru_{SA}/CNT (TOF_{1h} = 8 h^{-1}) and twice that of 1.2 % Ni_{NP}/CNT (TOF_{1h} = 306 h^{-1}). In addition, the S_{HCAL} reaches a value of 94.8 %, which is the highest obtained among all the investigated systems. It is worth mentioning that smaller Ni_{NP} supported on carbon are not expected to activate H_2 more easily than large NP.[88, 89] In addition, several works in the literature have shown that for hydrogenation reactions, an optimal size of Ni particles is around 10 nm; smaller particles being less active.[90, 91] Consequently, we did not believe that a Ni particle size effect can explain the higher performance of the $Ru_{SA}Ni_{NP}$/CNT catalyst compared to the Ni_{NP}/CNT catalyst.

Remarkably, S_{HCAL} remains very high even at high CAL conversion (Fig. 5), as a selectivity of 94 % to HCAL was achieved at 99 % CAL conversion with this catalyst at 100 °C and a pressure of 20 bar. In other words, the product selectivity was independent of conversion, which is generally not observed in this reaction with carbon-supported Ru catalysts.[92-95] This catalyst ranks above the Ru-based catalysts described in the literature, both in term of activity and HCAL selectivity.[4] It also shows good stability, since no modification in activity or selectivity was noted after five recycling experiments. It has been shown that the presence of Ru can promote the reduction of Ni oxides on Ni/CNT catalyst.[74] However, the increased performance of the $Ru_{SA}Ni_{NP}$/CNT catalyst compared to the Ni_{NP}/CNT catalyst cannot be attributed to a better

reduction of Ni in the bimetallic catalyst, since it is known that Ni/CNT catalyst prepared from nickel nitrate are efficiently reduced at 300 °C[73, 74].

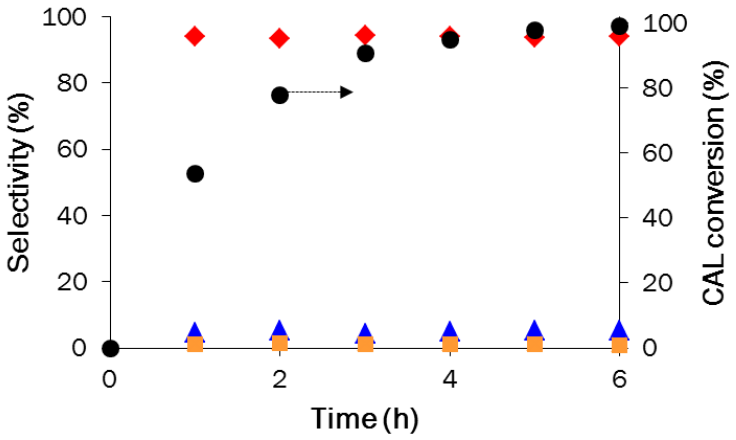

Figure 5. Evolution of CAL conversion and product selectivity on the 2 % $Ru_{SA}Ni_{NP}$/CNT catalyst. S_{HCAL} (red diamonds); S_{HCOL} (blue triangles); and S_{COL} (orange squares).

3.3. Operability of the $Ru_{SA}Ni_{NP}$/CNT catalyst in continuous flow

The $Ru_{SA}Ni_{NP}$/CNT catalyst has been wash coated on millimeter-scale NiCr foam substrates in order to test its ability in continuous flow operation (see experimental details for the procedures). These continuous tests are also interesting to discuss catalyst stability with easy access to relatively high turnover number (TON). Fig. S26 presents typical optical photographs of foam objects used in this study before and after the coating step. A relatively homogeneous covering has been obtained, also validated by SEM analyses (Fig. S27). STEM-HAADF analyses show that the coated $Ru_{SA}Ni_{NP}$/CNT catalyst has not been significantly affected by the coating process

(Fig. S28). A slight increase in Ni mean particle size (2 nm after coating for 1.3 nm before coating, Fig. S29) and decrease in SA/NP ratio (13 after coating for 17 before coating) were noticed. Continuous flow experiments have been performed for different liquid flow rates at constant temperature and constant pressure with an excess of hydrogen. Fig. 6 depicts the results obtained in this series of experiments. Fig. 6a and Fig. 6b show the evolution of CAL conversion with time on stream and the corresponding selectivity-conversion profile, respectively. It can be seen that a decrease in liquid flow rate tend to increase the CAL conversion and to decrease the HCAL selectivity in a scheme of consecutive reactions. It is noticeable that the decrease in selectivity starts at a lower conversion in continuous flow in comparison to the batch reactor. Non-ideal plug flow hydrodynamics with a small amount of liquid back-mixing may contribute to explained part of this result. Nonetheless, possible changes in the fine catalyst structure due to the coating process cannot be excluded but they were not sensible to the available characterizations techniques. It can be seen also that conversion is stable for each liquid flow rate, and a return to the initial flow rate of 1.0 mL min^{-1} at the end of the sequence leads to an identical conversion close to 30%. The results obtained can be reworked to be plotted as a function of contact time, typical of continuous catalytic reactor operation (Fig. 6c). This representation clearly makes appearing a linear behavior typical of a pseudo-zeroth order for CAL when conversions lower than 90% are obtained. This behavior tends to become closer to first order for the highest conversions (> 90%). The Site Time Yield (STY) observed in the continuous experiments is plotted against the Turn-Over Number (TON) in Fig. 6d. For the lower conversions, because of the pseudo-zeroth order, this average activity along the catalyst bed appears independent of the concentration (or conversion level) and is representative of the constant local activity.

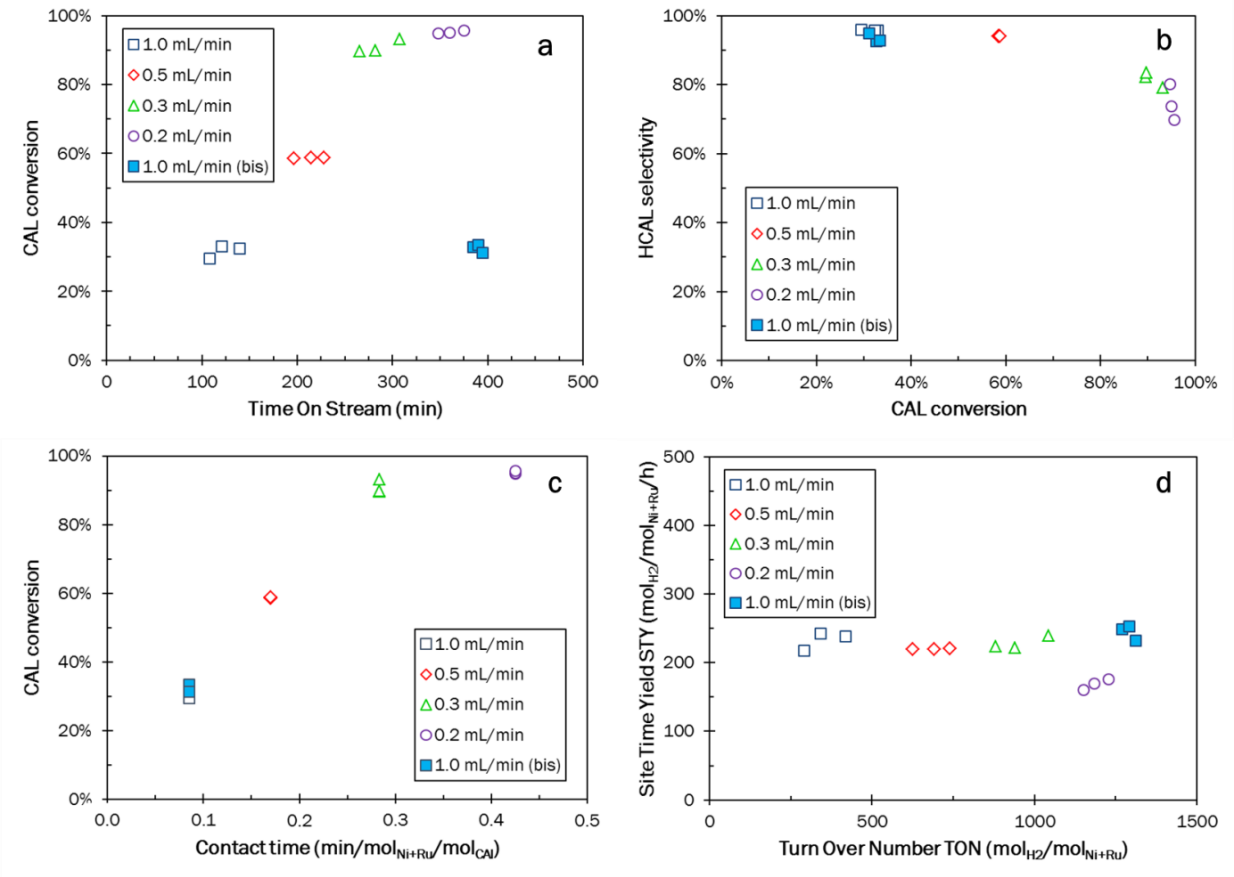

Figure 6. a) Time on stream evolution of CAL conversion in continuous flow experiments. **b**) Corresponding HCAL selectivity vs CAL conversion. **c**) Evolution of CAL conversion with contact time. **d**) Evolution of Site Time Yield (STY) with Turn-Over Number (TON).

A stable STY profile is obtained, up to a relatively important TON of 1300 mol_{H2} mol_{Ni+Ru}^{-1}, indicating a good stability of the coated catalyst. The lower STY obtained at a liquid flow rate of 0.2 mL min^{-1} is not to link with deactivation, but with the change in apparent order with the high conversion obtained at this point. This is confirmed with the control experiment repeated at 1.0 mL min^{-1} at the end of the sequence, where a similar STY is reached again. Overall, the catalyst

appears stable after the coating process, and can be operated in continuous flow, wash coated on structured internals.

Mechanistic study on the $Ru_{SA}Ni_{NP}$/CNT system

DFT calculations are used to understand whether the observed effect is related to the presence of activated isolated Ru_{SA} (*pathways B* - Ni_{NP}+Ru_{SA}) or to Ru atoms bound to the Ni_{NP} (*pathways D* - Ru_{SA}@Ni_{NP} in SAA catalyst). Consequently, the metal species present in the $Ru_{SA}Ni_{NP}$ SAA system are the Ni atoms of the Ni_{NP} and the Ru atom bound to the Ni_{NP} (Ru@Ni_{NP}) as a model of SAA (see Fig. 7 for the atomistic structure and Fig. S24 for a detailed electronic and electric characterization of the most stable catalyst model), as well as the activated isolated Ru_{SA}.

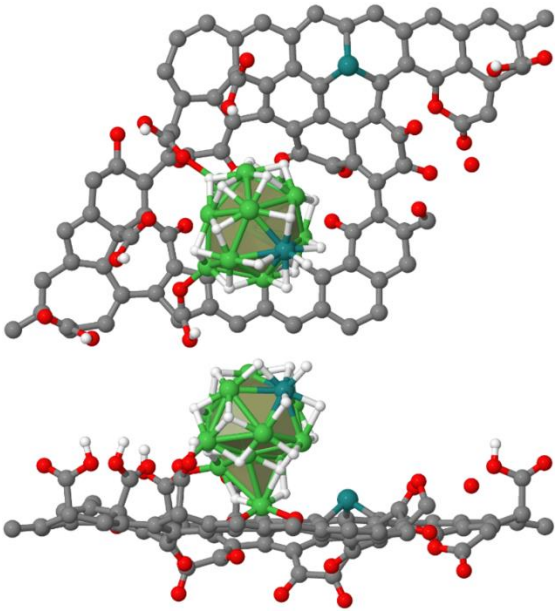

Figure 7. Top and side views of atomistic structure of the $Ru_{SA}Ni_{NP}$ SAA catalyst model. Atomic Color Scheme: Ru (Celadon Green); Ni (Apple); O (Candy Apple Red); C (Philippine Gray); H (White).

To further understand the experimental observations, the reaction mechanism for the selective hydrogenation of CAL on the three metal species of the SAA catalyst model is studied in the DFT framework. Starting from the role of nickel in Ni_{NP}, the coordination of 1,4-dioxane as the solvent used is first considered (see Fig. S30a), resulting in an adsorption energy of -21.4 kcal·mol^{-1}. After, the energy profile and the corresponding structures are summarized in Fig. S31 and Fig. S32, respectively (the energy profiles are presented as potential energies, thus, not considering entropies). On **3** (representing the $Ru_{SA}Ni_{NP}$ SAA catalyst model, see Fig. S31 and Fig. S32), the reaction begins by a π coordination of the alkene or carbonyl function of CAL. In both cases, the resulting intermediates are strongly adsorbed on the Ni_{NP} surface ($\mathbf{4}^{\mathbf{NP}}_{\mathbf{CHCH}}$ at -43.2 and $\mathbf{4}^{\mathbf{NP}}_{\mathbf{CHO}}$ at -35.8 kcal·mol^{-1}, respectively) by the π interaction of the double bond with a Ni atom (in a top adsorption site), and by the presence of two H-bonds between the organic substrate and -COOH functional groups of the support. Therefore, solvent molecules should be easily decoordinated from the Ni atoms by the presence of CAL.

Because the atoms forming the double bonds have different connectivity, the first H addition on both atoms is considered additionally for all studied cases. Additionally, given the high coverage conditions, where there are several H atoms around CAL, the H attacking the organic moiety is always the closest. From $\mathbf{4}^{\mathbf{NP}}_{\mathbf{CHCH}}$, the first hydrogenation step is thermodynamically relatively unfavorable on both carbon atoms, being the preferred on the carbon connected to –CHO group by about 10.8 kcal·mol^{-1} ($\mathbf{4}^{\mathbf{NP}}_{\mathbf{CHCH_2}}$, red pathway in Fig. S31). In both cases, the energy barrier is practically identical and around 40-42 kcal·mol^{-1}, so the first step is hardly achievable from the kinetic point of view. The situation changes particularly in terms of reaction energy for the second H addition ($\mathbf{4}^{\mathbf{NP}}_{\mathbf{CH_2CH_2}}$), favored by thermodynamics, regardless of the obtained reaction intermediate. The energy barriers, moreover, are notably lower than those of the first, around 15

kcal·mol^{-1}. On the other hand, starting from $\mathbf{4}^{\mathbf{NP}}_{\mathbf{CHO}}$, the first hydrogenation step is only slightly thermodynamically unfeasible on the oxygen atom ($\mathbf{4}^{\mathbf{NP}}_{\mathbf{CHOH}}$, dark yellow pathway in Fig. S31) by around 5.7 kcal·mol^{-1}, while the energy barriers remain kinetically difficult to access, at around 36-38 kcal mol^{-1}. Both thermodynamics and kinetics are favored in the second hydrogenation step of the C=O bond ($\mathbf{4}^{\mathbf{NP}}_{\mathbf{CH_2OH}}$), especially the latter, with drops in the energy barrier down to 15-25 kcal mol^{-1}. Once HCAL or COL is obtained, it is strongly coordinated on the surface (average desorption energy of 39 kcal·mol^{-1}) due to the interaction of Ni_{NP} with the aromatic ring through the η^2(C) coordination mode. Finally, the catalyst can be recharged under H_2 pressure by a thermodynamically favorable process. Therefore, the hydrogenation of CAL is difficult on Ni_{NP}, the first hydrogenation always being the most energy-demanding step.

Concerning the role of ruthenium in the $Ru_{SA}@Ni_{NP}$ SAA model, the coordination of the solvent 1,4-dioxane is only -1.9 kcal·mol^{-1} (see Fig. S30b), which gives the Ru atom greater availability as active site. The energy profiles and the corresponding structures are summarized in Fig. 8 (most favorable mechanisms), Fig. S33 (complete hydrogenation pathways), and Fig. S34, respectively. From **3** (Fig. S33 and Fig. S34), the adsorption of CAL ($\mathbf{4}^{\mathbf{SAA}}_{\mathbf{CHCH}}$ and $\mathbf{4}^{\mathbf{SAA}}_{\mathbf{CHO}}$ depending on the coordinating C=C or C=O function, respectively) is favorable from the thermodynamic point of view in both cases, and higher in the case of C=C coordination (binding energies of -23.8 and -14.0 kcal·mol^{-1}, respectively). The π coordination of the organic substrate on the Ru embedded in Ni_{NP} is very similar to those previously found on Ni_{NP}, while no H-bonds are observed since the active center is relatively far from the functionalized carbon support.

Once CAL is adsorbed, the possibility of first hydrogenating one carbon or another of the alkene group, as well as the carbon or oxygen atoms of the aldehyde group, opens up again. From a

thermodynamic point of view, the first hydrogenation turns out to be slightly endothermic for the C=C bond, and slightly exothermic for the C=O bond, with reaction energies between 0.7 ($\mathbf{4}^{\mathbf{SAA}}_{\mathbf{CH_2CH}}$, wine pathway in Fig. 8) and -2.2 kcal·mol^{-1} ($\mathbf{4}^{\mathbf{SAA}}_{\mathbf{CHOH}}$, dark yellow pathway in Fig. 8). The importance lies in the kinetics of the reaction, since both paths are energetically low. In fact, with an activation barrier of 16.9 kcal·mol^{-1}, hydrogenation of the easiest C atom of the alkene group can occur under operating conditions (temperature of 100 °C). However, the activation barrier of the aldehyde group (23.2 kcal·mol^{-1}), although also affordable, is above the desorption energy of the reactant (14.0 kcal·mol^{-1}). Therefore, a high activity on $Ru_{SA}@Ni_{NP}$ is expected with respect to C=C hydrogenation due to the low competition between the coordination of both functions, in addition to the C=O decoordination process. The second hydrogenation step of the alkene to obtain HCAL ($\mathbf{4}^{\mathbf{SAA}}_{\mathbf{CH_2CH_2}}$) is slightly disadvantaged from thermodynamics by 7.7 kcal·mol^{-1}, although the reaction kinetics are reasonably fast as in the first step (21.8 kcal·mol^{-1}). In the case where the first step of the aldehyde hydrogenation reaction takes place, the second step leading to the formation of COL ($\mathbf{4}^{\mathbf{SAA}}_{\mathbf{CH_2OH}}$) is thermodynamically favorable (-4.3 kcal·mol^{-1}), while from a kinetic viewpoint is also accessible with an energy barrier value of 14.1 kcal·mol^{-1}. Finally, the desorption of HCAL and COL from the $Ru_{SA}@Ni_{NP}$ site entails a low energy cost around 18.6 and 23.3 kcal·mol^{-1}, respectively, which further reinforces the preferential activity and selectivity of HCAL in the Ru-based SAAs.

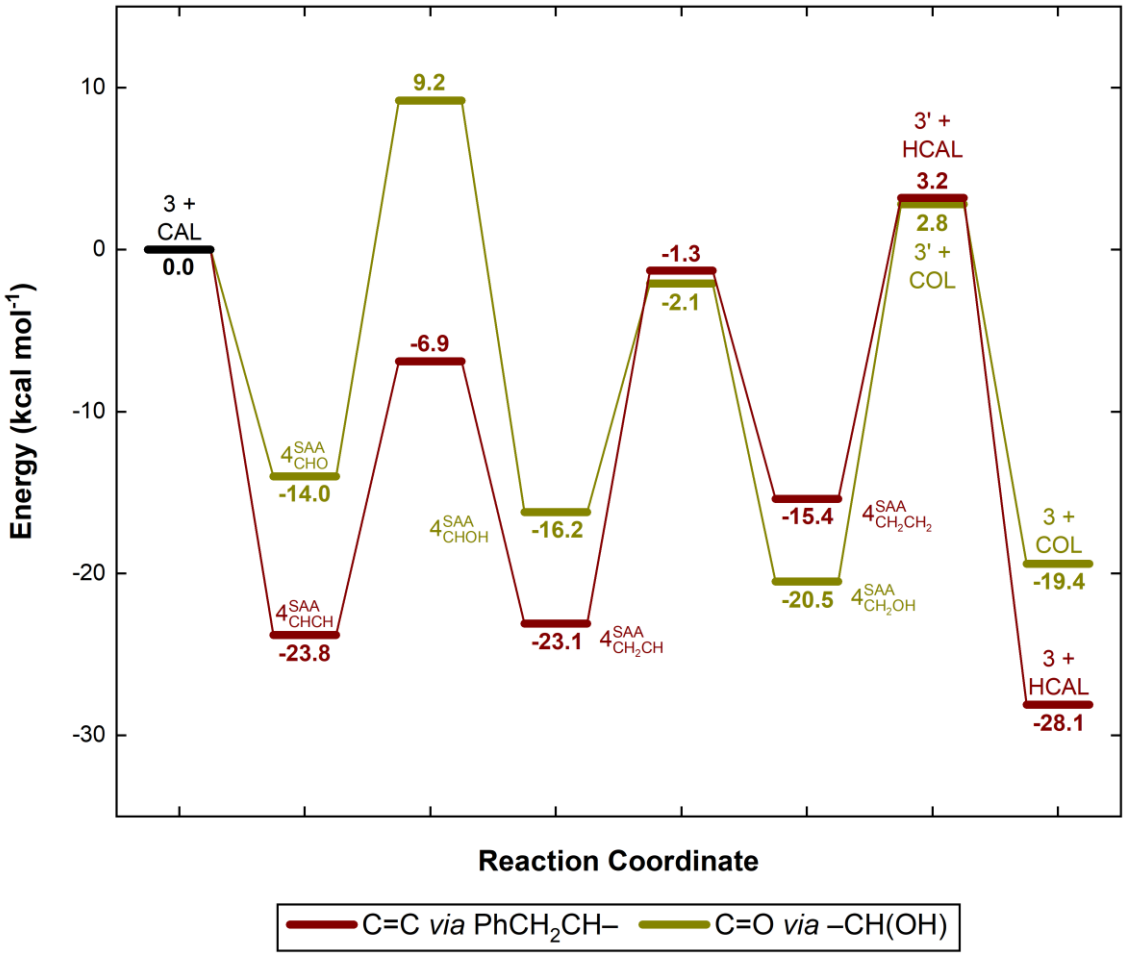

Figure 8. Reaction profile of CAL semi-hydrogenation to HCAL (in wine) and COL (in dark yellow) on the Ru@Ni_{NP} site of the $Ru_{SA}Ni_{NP}$ SAA catalyst model (black for the initial common step). The energy is referenced with respect to the hydrogenated (Ru–Ni)-supported catalyst (3) and $CAL_{(g)}$.

Regarding the role the isolated Ru_{SA} site of the $Ru_{SA}Ni_{NP}$ SAA system, the coordination of 1,4-dioxane on the Ru_{SA} and Ru_{SA}-H species is -31.2 and -4.1 kcal·mol^{-1}, respectively (see Fig. S30(c-d)), clearly chemisorbed in the case of the bare Ru_{SA}. Subsequently, the energy profiles and the corresponding structures are summarized in Fig. S35 and Fig. S36, respectively.

Unexpectedly, the formation of the active species Ru_{SA}-H by means of an H-spillover process ($\mathbf{3_H}$) turns out to be somewhat unfavorable from thermodynamics, unlike the $Ru_{SA}Ni_{NP}$ system (4.1 *vs* -7.0 kcal·mol^{-1}, respectively). The presence of the Ru atom on the Ni_{NP} is causing a subtle strengthening of the metal-H interactions, as in the case of the monometallic Ru_{SA+NP} system. The integrated pCOHP (IpCOHP), an average bond strength index, is 55.2, 25.7, and 27.1 kcal·mol^{-1} per metal-H interaction in the Ru_{SA+NP}, $Ru_{SA}Ni_{NP}$, and $Ru_{SA}Ni_{NP}$ SAA catalyst models, respectively. This fact limits the possibilities of Ru_{SA}-H being an active species for CAL hydrogenation. In the case of an H-spillover phenomenon (as experimentally evidenced, since some Ni_{NP} do not contain Ru), the reaction begins only by the favorable C=O bond coordination of CAL on Ru_{SA}-H ($\mathbf{4^{SA}_{H-CHO}}$, binding energy of -18.5 kcal·mol^{-1}). Coordination of the C=C bond is not observed, mainly because of steric hindrance, along with a preference for H-bonds with the support away from the Ru_{SA}. It should be noted that on Ru_{SA} only the η^1(O) coordination mode is observed, distinct from Ni_{NP} or Ru_{SA}@Ni_{NP}, for which the η^2(C=O) one is favored over others. Nevertheless, the study of CAL hydrogenation on Ru_{SA} is especially relevant to rule out the formation of COL in SAA catalysts, as observed experimentally.

Starting from $\mathbf{4^{SA}_{H-CHO}}$, the first hydrogenation step is a thermodynamically favorable process for both pathways, the average reaction energy being around -19 kcal·mol^{-1}. In contrast, neither pathway is kinetically easy, since although the lowest energy barrier is 28.3 kcal·mol^{-1}, the transition states of both pathways greatly exceed the adsorption energy of the organic substrate. In the case of being able to overcome them (thanks to the experimental reaction conditions), from any of the reaction intermediates, the second hydrogenation step proceeds exclusively by using molecular H_2 (wine and red pathways in Fig. S35). If a second H-spillover occurs, the processes would be energetically very unfavorable (orange and dark yellow pathways in Fig.

S35). Finally, hydrogenation thanks to dihydrogen could give rise to the formation of COL ($\mathbf{4}^{\mathbf{SA}}_{\mathbf{CH_2OH-H}}$), which remains coordinated through the hydroxyl group. According to these results, the isolated Ru_{SA} species seem not to be sufficiently active and, therefore, the production of the alcoholic compound is rather scarce.

4. CONCLUSIONS

Carbon nanotube supported Ru single atoms have been associated to metal nanoparticles (Ru, Pd, Ni) to probe H-spillover assisted cooperative catalysis in cinnamaldehyde hydrogenation. The Ru_{SA}/CNT catalyst shows poor performance for this reaction (TOF = 8 h^{-1}, S_{HCAL} = 73 %) due to its difficulty to active H_2. No cooperativity was observed when Ru_{SA} are associated to Ru_{NP} because H-spillover cannot operate in the Ru_{SA+NP}/CNT system for thermodynamic reasons. The performance of this catalyst (TOF = 181 h^{-1}, S_{HCAL} = 72 %) should be consequently associated to the Ru_{NP}. The association of Ru_{SA} to Pd_{NP} allows H-spillover to operate to produce Ru_{SA}-H species. For this $Ru_{SA}Pd_{NP}$/CNT catalyst, the selectivity towards HCAL is improved (S_{HCAL} = 90 %) compared to the Ru_{SA}/CNT (S_{HCAL} = 73 %) and Pd_{NP}/CNT systems (S_{HCAL} = 84 %). However, the very high activity of Pd_{NP} precludes probing the activity of Ru_{SA}-H species. The deposition of Ni on the Ru_{SA}/CNT catalyst results in a system containing two distinct Ru species: isolated Ru_{SA} and Ru_{SA} associated to Ni_{NP} (Ru_{SA}@Ni_{NP}, SAA). The hydrogen spillover from Ni_{NP} to isolated Ru_{SA} can operate but is not favorable from Ru_{SA}@Ni_{NP} to Ru_{SA}. The $Ru_{SA}Ni_{NP}$/CNT catalyst shows much better performances in terms of activity and selectivity compared to the Ru_{SA}/CNT and Ni_{NP}/CNT systems. This $Ru_{SA}Ni_{NP}$/CNT catalyst also shows excellent recyclability and promising performances in a lab-scale flow reactor. DFT calculations

revealed that the selective hydrogenation of CAL to HCAL is a slightly endothermic reaction, kinetically accessible only by the Ru site on the $Ru_{SA}@Ni_{NP}$ single atom alloys. The Ru_{SA}-H species does not allow HCAL formation due to steric reasons, however it favors the production of COL through a kinetically limited pathway. In the SAA, the activation barriers for the hydrogenation reaction on $Ru_{SA}@Ni_{NP}$ (21.8 kcal·mol^{-1}) is much lower than on Ni_{NP} (39.5 kcal·mol^{-1}). The introduction of Ru_{SA} on the Ni_{NP} greatly reduced the barriers necessary for the first H addition and the HCAL desorption.

Acknowledgement

This work was supported by the Agence Nationale de la Recherche (ANR-19-CE07-0030, COMET), which is gratefully acknowledged. The authors also thankfully acknowledge the HPC resources at CINES and IDRIS under the allocation 2021-A0100906649 made by GENCI. We also thank the Diamond Light Source for the award of beam time as part of the Energy Materials Block Allocation Group SP14239. J.N.-R., I.D.R., and I.C.G. acknowledge the "Calcul en Midi-Pyrénées" initiative CALMIP (projects p0812 and p1214) for the computer resources. We thank Vincent Collière (LCC, UPR8241 CNRS, Toulouse, France) for STEM analysis.

Funding Sources

Agence Nationale de la Recherche (ANR-19-CE07-0030, COMET).

Footnote

‡These authors contributed equally.

References

[1] X. Lan, T. Wang, Highly Selective Catalysts for the Hydrogenation of Unsaturated Aldehydes: A Review, ACS Catalysis, 10 (2020) 2764-2790.

[2] X. Wang, X. Liang, P. Geng, Q. Li, Recent Advances in Selective Hydrogenation of Cinnamaldehyde over Supported Metal-Based Catalysts, ACS Catalysis, 10 (2020) 2395-2412.

[3] P. Gallezot, D. Richard, Selective Hydrogenation of α,β-Unsaturated Aldehydes, Catalysis Reviews, 40 (1998) 81-126.

[4] F. Leng, I.C. Gerber, M.R. Axet, P. Serp, Selectivity shifts in hydrogenation of cinnamaldehyde on electron-deficient ruthenium nanoparticles, Comptes Rendus Chimie, 21 (2018) 346-353.

[5] Z. Tian, Q. Li, Y. Li, S. Ai, Synthesis of nitrogen-doped carbon coated TiO2 microspheres and its application as metal support in cinnamaldehyde hydrogenation, Catalysis Communications, 61 (2015) 97-101.

[6] C. Louis, L. Delannoy, Chapter One - Selective hydrogenation of polyunsaturated hydrocarbons and unsaturated aldehydes over bimetallic catalysts, in: C. Song (Ed.) Advances in Catalysis, Academic Press, 2019, pp. 1-88.

[7] M. Luneau, J.S. Lim, D.A. Patel, E.C.H. Sykes, C.M. Friend, P. Sautet, Guidelines to Achieving High Selectivity for the Hydrogenation of α,β-Unsaturated Aldehydes with Bimetallic and Dilute Alloy Catalysts: A Review, Chemical Reviews, 120 (2020) 12834-12872.

[8] R. Prins, Hydrogen Spillover. Facts and Fiction, Chemical Reviews, 112 (2012) 2714-2738.

[9] M.M. Bettahar, The hydrogen spillover effect. A misunderstanding story, Catalysis Reviews, 64 (2022) 87-125.

[10] S. Wu, K.-Y. Tseng, R. Kato, T.-S. Wu, A. Large, Y.-K. Peng, W. Xiang, H. Fang, J. Mo, I. Wilkinson, Y.-L. Soo, G. Held, K. Suenaga, T. Li, H.-Y.T. Chen, S.C.E. Tsang, Rapid Interchangeable Hydrogen, Hydride, and Proton Species at the Interface of Transition Metal Atom on Oxide Surface, Journal of the American Chemical Society, 143 (2021) 9105-9112.

[11] L. Wang, R.T. Yang, Hydrogen Storage on Carbon-Based Adsorbents and Storage at Ambient Temperature by Hydrogen Spillover, Catalysis Reviews, 52 (2010) 411-461.

[12] M. Mohan, V.K. Sharma, E.A. Kumar, V. Gayathri, Hydrogen storage in carbon materials—A review, Energy Storage, 1 (2019) e35.

[13] U. Roland, T. Braunschweig, F. Roessner, On the nature of spilt-over hydrogen, Journal of Molecular Catalysis A: Chemical, 127 (1997) 61-84.

[14] F. Yang, B. Hu, W. Xia, B. Peng, J. Shen, M. Muhler, On the nature of spillover hydrogen species on platinum/nitrogen-doped mesoporous carbon composites: A temperature-programmed nitrobenzene desorption study, Journal of Catalysis, 365 (2018) 55-62.

[15] W. Lin, H. Cheng, L. He, Y. Yu, F. Zhao, High performance of Ir-promoted Ni/TiO2 catalyst toward the selective hydrogenation of cinnamaldehyde, Journal of Catalysis, 303 (2013) 110-116.

[16] K. Taniya, H. Jinno, M. Kishida, Y. Ichihashi, S. Nishiyama, Preparation of Sn-modified silica-coated Pt catalysts: A new PtSn bimetallic model catalyst for selective hydrogenation of crotonaldehyde, Journal of Catalysis, 288 (2012) 84-91.

[17] L. Zhang, M. Zhou, A. Wang, T. Zhang, Selective Hydrogenation over Supported Metal Catalysts: From Nanoparticles to Single Atoms, Chemical Reviews, 120 (2020) 683-733.

[18] Z. Sun, S. Wang, W. Chen, Metal single-atom catalysts for selective hydrogenation of unsaturated bonds, Journal of Materials Chemistry A, 9 (2021) 5296-5319.

[19] Z. Li, X. Dong, M. Zhang, L. Leng, W. Chen, J.H. Horton, J. Wang, Z. Li, W. Wu, Selective Hydrogenation on a Highly Active Single-Atom Catalyst of Palladium Dispersed on Ceria Nanorods by Defect Engineering, ACS Applied Materials & Interfaces, 12 (2020) 57569-57577.

[20] H. Yan, H. Lv, H. Yi, W. Liu, Y. Xia, X. Huang, W. Huang, S. Wei, X. Wu, J. Lu, Understanding the underlying mechanism of improved selectivity in pd1 single-atom catalyzed hydrogenation reaction, Journal of Catalysis, 366 (2018) 70-79.

[21] Z. Li, W. Wei, H. Li, S. Li, L. Leng, M. Zhang, J.H. Horton, D. Wang, W. Sun, C. Guo, W. Wu, J. Wang, Low-Temperature Synthesis of Single Palladium Atoms Supported on Defective Hexagonal Boron Nitride Nanosheet for Chemoselective Hydrogenation of Cinnamaldehyde, ACS Nano, 15 (2021) 10175-10184.

[22] L. Ning, S. Liao, H. Li, R. Tong, C. Dong, M. Zhang, W. Gu, X. Liu, Carbon-based materials with tunable morphology confined Ni (0) and Ni-Nx active sites: Highly efficient selective hydrogenation catalysts, Carbon, 154 (2019) 48-57.

[23] C. Rivera-Cárcamo, I.C. Gerber, I. del Rosal, B. Guicheret, R. Castro Contreras, L. Vanoye, A. Favre-Réguillon, B.F. Machado, J. Audevard, C. de Bellefon, R. Philippe, P. Serp, Control of the single atom/nanoparticle ratio in Pd/C catalysts to optimize the cooperative hydrogenation of alkenes, Catalysis Science & Technology, 11 (2021) 984-999.

[24] L. Kuai, Z. Chen, S. Liu, E. Kan, N. Yu, Y. Ren, C. Fang, X. Li, Y. Li, B. Geng, Titania supported synergistic palladium single atoms and nanoparticles for room temperature ketone and aldehydes hydrogenation, Nature Communications, 11 (2020) 48.

[25] X. Lu, C. Guo, M. Zhang, L. Leng, J.H. Horton, W. Wu, Z. Li, Rational design of palladium single-atoms and clusters supported on silicoaluminophosphate-31 by a photochemical route for chemoselective hydrodeoxygenation of vanillin, Nano Research, 14 (2021) 4347-4355.
[26] Y. Cao, B. Chen, J. Guerrero-Sánchez, I. Lee, X. Zhou, N. Takeuchi, F. Zaera, Controlling Selectivity in Unsaturated Aldehyde Hydrogenation Using Single-Site Alloy Catalysts, ACS Catalysis, 9 (2019) 9150-9157.
[27] Y. Cao, J. Guerrero-Sańchez, I. Lee, X. Zhou, N. Takeuchi, F. Zaera, Kinetic Study of the Hydrogenation of Unsaturated Aldehydes Promoted by CuPtx/SBA-15 Single-Atom Alloy (SAA) Catalysts, ACS Catalysis, 10 (2020) 3431-3443.
[28] K.-Q. Sun, Y.-C. Hong, G.-R. Zhang, B.-Q. Xu, Synergy between Pt and Au in Pt-on-Au Nanostructures for Chemoselective Hydrogenation Catalysis, ACS Catalysis, 1 (2011) 1336-1346.
[29] L. Vanoye, B. Guicheret, C. Rivera-Cárcamo, R. Castro Contreras, C. de Bellefon, V. Meille, P. Serp, R. Philippe, A. Favre-Réguillon, Process intensification of the catalytic hydrogenation of squalene using a Pd/CNT catalyst combining nanoparticles and single atoms in a continuous flow reactor, Chemical Engineering Journal, 441 (2022) 135951.
[30] J. Audevard, A. Benyounes, R. Castro Contreras, H. Abou Oualid, M. Kacimi, P. Serp, Multifunctional Catalytic Properties of Pd/CNT Catalysts for 4-Nitrophenol Reduction, ChemCatChem, 14 (2022) e202101783.
[31] P. Serp, Cooperativity in supported metal single atom catalysis, Nanoscale, 13 (2021) 5985-6004.
[32] B. Guicheret, L. Vanoye, C. Rivera-Cárcamo, C. de Bellefon, P. Serp, R. Philippe, A. Favre-Réguillon, Solvent-Free Hydrogenation of Squalene Using Parts per Million Levels of

Palladium Supported on Carbon Nanotubes: Shift from Batch Reactor to Continuous-Flow System, ChemSusChem, 15 (2022) e202200916.

[33] C. Rivera-Cárcamo, C. Scarfiello, A.B. García, Y. Tison, H. Martinez, W. Baaziz, O. Ersen, C. Le Berre, P. Serp, Stabilization of Metal Single Atoms on Carbon and TiO2 Supports for CO2 Hydrogenation: The Importance of Regulating Charge Transfer, Advanced Materials Interfaces, 8 (2021) 2001777.

[34] B. Ravel, M. Newville, ATHENA, ARTEMIS, HEPHAESTUS: data analysis for X-ray absorption spectroscopy using IFEFFIT, Journal of Synchrotron Radiation, 12 (2005) 537-541.

[35] A. Borodziński, M. Bonarowska, Relation between Crystallite Size and Dispersion on Supported Metal Catalysts, Langmuir, 13 (1997) 5613-5620.

[36] F. Simescu-Lazar, T. Chaieb, S. Pallier, L. Veyre, R. Philippe, V. Meille, Direct coating of carbon-supported catalysts on monoliths and foams – Singular behaviour of Pd/MWCNT, Applied Catalysis A: General, 508 (2015) 45-51.

[37] S. Khoobiar, Particle to Particle Migration of Hydrogen Atoms on Platinum—Alumina Catalysts from Particle to Neighboring Particles, The Journal of Physical Chemistry, 68 (1964) 411-412.

[38] G. Kresse, J. Furthmüller, Efficiency of ab-initio total energy calculations for metals and semiconductors using a plane-wave basis set, Computational Materials Science, 6 (1996) 15-50.

[39] G. Kresse, J. Furthmüller, Efficient iterative schemes for ab initio total-energy calculations using a plane-wave basis set, Physical Review B, 54 (1996) 11169-11186.

[40] J.P. Perdew, K. Burke, M. Ernzerhof, Generalized Gradient Approximation Made Simple, Physical Review Letters, 77 (1996) 3865-3868.

[41] S. Grimme, J. Antony, S. Ehrlich, H. Krieg, A consistent and accurate ab initio parametrization of density functional dispersion correction (DFT-D) for the 94 elements H-Pu, The Journal of Chemical Physics, 132 (2010) 154104.

[42] P.E. Blöchl, Projector augmented-wave method, Physical Review B, 50 (1994) 17953-17979.

[43] G. Kresse, D. Joubert, From ultrasoft pseudopotentials to the projector augmented-wave method, Physical Review B, 59 (1999) 1758-1775.

[44] J. Navarro-Ruiz, C. Rivera-Cárcamo, B. Machado, P. Serp, I. Del Rosal, I.C. Gerber, Computational Design of Pd Nanoclusters and Pd Single-Atom Catalysts Supported on O-Functionalized Graphene, ACS Applied Nano Materials, 4 (2021) 12235-12249.

[45] H.J. Monkhorst, J.D. Pack, Special points for Brillouin-zone integrations, Physical Review B, 13 (1976) 5188-5192.

[46] G. Makov, M.C. Payne, Periodic boundary conditions in ab initio calculations, Physical Review B, 51 (1995) 4014-4022.

[47] G. Henkelman, H. Jónsson, Improved tangent estimate in the nudged elastic band method for finding minimum energy paths and saddle points, The Journal of Chemical Physics, 113 (2000) 9978-9985.

[48] G. Henkelman, B.P. Uberuaga, H. Jónsson, A climbing image nudged elastic band method for finding saddle points and minimum energy paths, The Journal of Chemical Physics, 113 (2000) 9901-9904.

[49] I.C. Gerber, P. Serp, A Theory/Experience Description of Support Effects in Carbon-Supported Catalysts, Chemical Reviews, 120 (2020) 1250-1349.

[50] U. Petek, F. Ruiz-Zepeda, M. Bele, M. Gaberščček, Nanoparticles and Single Atoms in Commercial Carbon-Supported Platinum-Group Metal Catalysts, Catalysts, 9 (2019) 134.
[51] L. Liu, A. Corma, Identification of the active sites in supported subnanometric metal catalysts, Nature Catalysis, 4 (2021) 453-456.
[52] C. Rivera-Cárcamo, F. Leng, I.C. Gerber, I. del Rosal, R. Poteau, V. Collière, P. Lecante, D. Nechiyil, W. Bacsa, A. Corrias, M.R. Axet, P. Serp, Catalysis to discriminate single atoms from subnanometric ruthenium particles in ultra-high loading catalysts, Catalysis Science & Technology, 10 (2020) 4673-4683.
[53] C.-T. Kuo, Y. Lu, L. Kovarik, M. Engelhard, A.M. Karim, Structure Sensitivity of Acetylene Semi-Hydrogenation on Pt Single Atoms and Subnanometer Clusters, ACS Catalysis, 9 (2019) 11030-11041.
[54] C. Liu, K.S. Kim, J. Baek, Y. Cho, S. Han, S.-W. Kim, N.-K. Min, Y. Choi, J.-U. Kim, C.J. Lee, Improved field emission properties of double-walled carbon nanotubes decorated with Ru nanoparticles, Carbon, 47 (2009) 1158-1164.
[55] J.V. Rojas, M. Toro-Gonzalez, M.C. Molina-Higgins, C.E. Castano, Facile radiolytic synthesis of ruthenium nanoparticles on graphene oxide and carbon nanotubes, Materials Science and Engineering: B, 205 (2016) 28-35.
[56] K. Jiang, H. Wang, Electrocatalysis over Graphene-Defect-Coordinated Transition-Metal Single-Atom Catalysts, Chem, 4 (2018) 194-195.
[57] L. Zhang, J.M. Winterbottom, A.P. Boyes, S. Raymahasay, Studies on the hydrogenation of cinnamaldehyde over Pd/C catalysts, Journal of Chemical Technology & Biotechnology, 72 (1998) 264-272.

[58] B. Gerand, M. Figlarz, Reduction of Hexagonal WO3 by Hydrogen Spillover : Formation of New Hydrogen Hexagonal Tungsten Bronzes HxWO3, in: G.M. Pajonk, S.J. Teichner, J.E. Germain (Eds.) Studies in Surface Science and Catalysis, Elsevier, 1983, pp. 275-283.

[59] S.K. Konda, A. Chen, Palladium based nanomaterials for enhanced hydrogen spillover and storage, Materials Today, 19 (2016) 100-108.

[60] X. Kong, J. Xiao, A. Chen, L. Chen, C. Li, L. Feng, X. Ren, X. Fan, W. Sun, Z. Sun, Enhanced Catalytic Denitrification Performance of Ruthenium-based Catalysts by Hydrogen Spillover from a Palladium Promoter, Journal of Colloid and Interface Science, 608 (2022) 2973-2984.

[61] J. Qiu, H. Zhang, X. Wang, H. Han, C. Liang, C. Li, Selective hydrogenation of cinnamaldehyde over carbon nanotube supported pd-ru catalyst, Reaction Kinetics and Catalysis Letters, 88 (2006) 269-276.

[62] V.V. Rozanov, O.V. Krylov, Hydrogen spillover in heterogeneous catalysis, Russian Chemical Reviews, 66 (1997) 107-119.

[63] V. Almasan, T. Gaeumann, M. Lazar, P. Marginean, N. Aldea, Hydrogen spillover effect over the oxide surfaces in supported nickel catalysts, in: G.F. Froment, K.C. Waugh (Eds.) Studies in Surface Science and Catalysis, Elsevier, 1997, pp. 547-552.

[64] M. Zieliński, R. Wojcieszak, S. Monteverdi, M. Mercy, M.M. Bettahar, Hydrogen storage in nickel catalysts supported on activated carbon, International Journal of Hydrogen Energy, 32 (2007) 1024-1032.

[65] Y.-J. Han, S.-J. Park, Influence of nickel nanoparticles on hydrogen storage behaviors of MWCNTs, Applied Surface Science, 415 (2017) 85-89.

[66] R. Wojcieszak, M. Zieliński, S. Monteverdi, M.M. Bettahar, Study of nickel nanoparticles supported on activated carbon prepared by aqueous hydrazine reduction, Journal of Colloid and Interface Science, 299 (2006) 238-248.

[67] L. Zhu, H. Zhang, N. Ma, C. Yu, N. Ding, J.-L. Chen, C.-W. Pao, J.-F. Lee, Q. Xiao, B. Hui Chen, Tuning the interfaces in the ruthenium-nickel/carbon nanocatalysts for enhancing catalytic hydrogenation performance, Journal of Catalysis, 377 (2019) 299-308.

[68] T. Miyata, M. Shiraga, D. Li, I. Atake, T. Shishido, Y. Oumi, T. Sano, K. Takehira, Promoting effect of Ru on Ni/Mg(Al)O catalysts in DSS-like operation of CH4 steam reforming, Catalysis Communications, 8 (2007) 447-451.

[69] C. Li, M. Yang, Z. Liu, Z. Zhang, T. Zhu, X. Chen, Y. Dong, H. Cheng, Ru–Ni/Al_2O_3 bimetallic catalysts with high catalytic activity for N-propylcarbazole hydrogenation, Catalysis Science & Technology, 10 (2020) 2268-2276.

[70] V.S. Guggilla, J. Akyurtlu, A. Akyurtlu, I. Blankson, Steam Reforming of n-Dodecane over Ru−Ni-Based Catalysts, Industrial & Engineering Chemistry Research, 49 (2010) 8164-8173.

[71] Z.-F. Zhao, Z.-J. Wu, L.-X. Zhou, M.-H. Zhang, W. Li, K.-Y. Tao, Synthesis of a nano-nickel catalyst modified by ruthenium for hydrogenation and hydrodechlorination, Catalysis Communications, 9 (2008) 2191-2194.

[72] A. Sreenavya, C.N. Mallannavar, A. Sakthivel, Functional group hydrogenation of cinnamaldehyde to hydrocinnamyl alcohol over nickel-ruthenium containing hydrotalcite, Materials Today: Proceedings, 46 (2021) 3152-3157.

[73] L.F. Sosa, V.T. da Silva, P.M. de Souza, Hydrogenation of levulinic acid to γ-valerolactone using carbon nanotubes supported nickel catalysts, Catalysis Today, 381 (2021) 86-95.

[74] L.S. Ribeiro, J.J. Delgado, J.J.M. Órfão, M.F.R. Pereira, Carbon supported Ru-Ni bimetallic catalysts for the enhanced one-pot conversion of cellulose to sorbitol, Applied Catalysis B: Environmental, 217 (2017) 265-274.
[75] Q. Ma, D. Wang, M. Wu, T. Zhao, Y. Yoneyama, N. Tsubaki, Effect of catalytic site position: Nickel nanocatalyst selectively loaded inside or outside carbon nanotubes for methane dry reforming, Fuel, 108 (2013) 430-438.
[76] F. Tian, M. Zhang, X. Zhang, X. Chen, J. Wang, Y. Zhang, C. Meng, C. Liang, Porous carbon-encapsulated Ni nanocatalysts for selective catalytic hydrogenation of cinnamaldehyde to hydrocinnamaldehyde, Journal of Materials Science, 57 (2022) 3168-3182.
[77] P. Johar, C.R. McElroy, E.L. Rylott, A.S. Matharu, J.H. Clark, Biologically bound nickel as a sustainable catalyst for the selective hydrogenation of cinnamaldehyde, Applied Catalysis B: Environmental, 306 (2022) 121105.
[78] S. Gryglewicz, A. Śliwak, J. Ćwikła, G. Gryglewicz, Performance of Carbon Nanofiber and Activated Carbon Supported Nickel Catalysts for Liquid-Phase Hydrogenation of Cinnamaldehyde into Hydrocinnamaldehyde, Catalysis Letters, 144 (2014) 62-69.
[79] H. Wang, Q. Luo, W. Liu, Y. Lin, Q. Guan, X. Zheng, H. Pan, J. Zhu, Z. Sun, S. Wei, J. Yang, J. Lu, Quasi Pd1Ni single-atom surface alloy catalyst enables hydrogenation of nitriles to secondary amines, Nature Communications, 10 (2019) 4998.
[80] W. Liu, H. Feng, Y. Yang, Y. Niu, L. Wang, P. Yin, S. Hong, B. Zhang, X. Zhang, M. Wei, Highly-efficient RuNi single-atom alloy catalysts toward chemoselective hydrogenation of nitroarenes, Nature Communications, 13 (2022) 3188.

[81] G.B. Kasar, R.S. Medhekar, P.N. Bhosale, C.V. Rode, Kinetics of Hydrogenation of Aqueous Levulinic Acid over Bimetallic Ru–Ni/MMT Catalyst, Industrial & Engineering Chemistry Research, 58 (2019) 19803-19817.

[82] Y. Pan, X. Han, X. Chang, H. Zhang, X. Zi, Z. Hao, J. Chen, Z. Lin, M. Li, X. Ma, Enhanced Low-Temperature CO_2 Methanation over Bimetallic Ni–Ru Catalysts, Industrial & Engineering Chemistry Research, (2023).

[83] S. Shao, Y. Yang, K. Sun, S. Yang, A. Li, F. Yang, X. Luo, S. Hao, Y. Ke, Electron-Rich Ruthenium Single-Atom Alloy for Aqueous Levulinic Acid Hydrogenation, ACS Catalysis, 11 (2021) 12146-12158.

[84] S. Oswald, W. Brückner, XPS depth profile analysis of non-stoichiometric NiO films, Surface and Interface Analysis, 36 (2004) 17-22.

[85] H. Wang, X. Kou, L. Zhang, J. Li, Size-controlled synthesis, microstructure and magnetic properties of Ni nanoparticles, Materials Research Bulletin, 43 (2008) 3529-3536.

[86] V. Vonk, N. Khorshidi, A. Stierle, Structure and Oxidation Behavior of Nickel Nanoparticles Supported by YSZ(111), The Journal of Physical Chemistry C, 121 (2017) 2798-2806.

[87] G.E. Haslam, K. Sato, T. Mizokawa, X.-Y. Chin, G.T. Burstein, Charge transfer effects in electrocatalytic Ni-C revealed by x-ray photoelectron spectroscopy, Applied Physics Letters, 100 (2012) 231601.

[88] S. Amaya-Roncancio, A.A. García Blanco, D.H. Linares, K. Sapag, DFT study of hydrogen adsorption on Ni/graphene, Applied Surface Science, 447 (2018) 254-260.

[89] B. Liu, M.T. Lusk, J.F. Ely, Influence of Nickel Catalyst Geometry on the Dissociation Barriers of H2 and CH4: Ni13 versus Ni(111), The Journal of Physical Chemistry C, 113 (2009) 13715-13722.

[90] Y. Fu, F. Devred, P. Eloy, T. Haynes, M.L. Singleton, S. Hermans, The effect of Ni particle size and carbon support on catalytic activity for glucose hydrogenation reaction, Applied Catalysis A: General, 644 (2022) 118833.

[91] N.L. Visser, O. Daoura, P.N. Plessow, L.C.J. Smulders, J.W. de Rijk, J.A. Stewart, B.D. Vandegehuchte, F. Studt, J.E.S. van der Hoeven, P.E. de Jongh, Particle Size Effects of Carbon Supported Nickel Nanoparticles for High Pressure CO2 Methanation, ChemCatChem, 14 (2022) e202200665.

[92] S. Galvagno, G. Capannelli, G. Neri, A. Donato, R. Pietropaolo, Hydrogenation of cinnamaldehyde over Ru/C catalysts: effect of Ru particle size, Journal of Molecular Catalysis, 64 (1991) 237-246.

[93] A. Giroir-Fendler, D. Richard, P. Gallezot, Selectivity in Cinnamaldehyde Hydrogenation of Group-VIII Metals Supported on Graphite and Carbon, in: M. Guisnet, J. Barrault, C. Bouchoule, D. Duprez, C. Montassier, G. Pérot (Eds.) Studies in Surface Science and Catalysis, Elsevier, 1988, pp. 171-178.

[94] A.J. Plomp, H. Vuori, A.O.I. Krause, K.P. de Jong, J.H. Bitter, Particle size effects for carbon nanofiber supported platinum and ruthenium catalysts for the selective hydrogenation of cinnamaldehyde, Applied Catalysis A: General, 351 (2008) 9-15.

[95] M. Lashdaf, A. Hase, E. Kauppinen, A.O.I. Krause, Fullerene-based ruthenium catalysts in cinnamaldehyde hydrogenation, Catalysis Letters, 52 (1998) 199-204.